Relationships between volcano gravitational spreading and magma intrusion

Audray Delcamp · Benjamin van Wyk de Vries · Mike R. James · L. S. Gailler · E. Lebas

Abstract Volcano spreading, with its characteristic sector grabens, is caused by outward flow of weak substrata due to gravitational loading. This process is now known to affect many present-day edifices. A volcano intrusive complex can form an important component of an edifice and may induce deformation while it develops. Such intrusions are clearly observed in ancient eroded volcanoes, like the Scottish Palaeocene centres, or in geophysical studies such as in La Réunion, or inferred from large calderas, such as in Hawaii, the Canaries or Galapagos volcanoes. Volcano gravitational spreading and intrusive complex emplacement may act simultaneously within an edifice. We explore the coupling and interactions between these two processes. We use scaled analogue models, where an intrusive complex made of Golden syrup is emplaced within a granular model volcano based on a substratum of a ductile silicone layer overlain by a brittle granular layer. We model specifically the large intrusive complex growth and do not model small-scale and short-lived events, such as dyke intrusion, that develop above the intrusive complex. The models show that the intrusive complex develops in continual competition between upward bulging and lateral gravity spreading. The brittle substratum strongly controls the deformation style, the intrusion shape and also controls the balance between intrusive complex spreading and ductile layer-related gravitational spreading. In the models, intrusive complex emplacement and spreading produce similar structures to those formed during volcano gravitational spreading alone (i.e. grabens, folds, en échelon fractures). Therefore, simple analysis of fault geometry and fault kinetic indicators is not sufficient to distinguish gravitational from intrusive complex spreading, except when the intrusive complex is eccentric from the volcano centre. However, the displacement fields obtained for (1) a solely gravitational spreading volcano and for (2) a gravitational spreading volcano with a growing and spreading intrusive complex are very different. Consequently, deformation fields (like those obtained from geodetic monitoring) can give a strong indication of the presence of a spreading intrusive complex. We compare the models with field observations and geophysical evidence on active volcanoes such as La Réunion Island (Indian Ocean), Ometepe Island (Nicaragua) and eroded volcanic remnants such as Ardnamurchan (Scotland) and suggest that a combination between gravitational and intrusive complex spreading has been active.

Keywords Volcano · Intrusive complex · Spreading · Gravitational spreading · Rift zone · Analogue models

A. Delcamp · B. van Wyk de Vries · L. S. Gailler · E. Lebas
Laboratoire Magmas et Volcans CNRS-UMR 6524,
Observatoire du Physique du Globe de Clermont,
Université Blaise Pascal,
Clermont-Ferrand, France

B. van Wyk de Vries
e-mail: b.vanwyk@opgc.univ-bpclermont.fr

A. Delcamp (✉)
Department of Geography, Earth System Sciences,
Vrije Universiteit Brussel,
Brussel, Belgium
e-mail: delcampa@tcd.ie

M. R. James
Lancaster Environment Centre, Lancaster University,
Lancaster, UK
e-mail: m.james@lancs.ac.uk

Introduction

Intrusions such as dykes, sills, cone sheets and intrusive complexes can constitute an important part of volcano

architecture and growth (e.g. Francis et al. 1993; Annen et al. 2001; Mathieu and van Wyk de Vries 2009). While dykes and sills are important near-surface intrusions and are regularly detected by geodetic monitoring, large-scale intrusive complex growth provides long-term, large-scale deformation that can be seen on large volcanoes, such as Hawaii and Etna (e.g. Delaney et al. 1990; Clague and Denlinger 1994; Chiocci et al. 2011). Large intrusive complexes clearly develop inside volcanoes, as seen in eroded volcanoes (such as the Scottish Palaeocene centres of Arndamurchan, Sky, Mull, Arran and Rum). They are also detected by geophysical evidence, such as at La Réunion Island (Gailler et al. 2009; Gailler and Lénat 2010), and from the presence of large calderas, as observed on most large volcanoes (Roche et al. 2001).

Intrusion emplacement can induce surface deformation on a volcano, in the extreme like the bulge observed at Mount St. Helens prior to the May 1980 eruption, or during inflation and dyke intrusion episodes at volcanoes such as Hawaii or Piton de la Fournaise (Swanson et al. 1976; Dieterich 1988; Cayol et al. 2000; Brooks et al. 2008). Intrusive complex emplacement induces also deformation in the host rock. For example, in the Ardnamurchan Peninsula, Scotland, the surrounding sediments, schists and volcanic rocks are folded around the intrusive complex (Bailey et al. 1924; Tyrell 1928).

Volcano spreading is the lateral deformation of the volcano edifice along a basal ductile layer that deforms under the volcano weight. This mechanism has been widely studied on the field (van Bemmelen 1949; Borgia et al. 1992, 2000; Borgia and van Wyk de Vries 2003) and using analogue and numerical modelling (Merle and Borgia 1996; van Wyk and Matela 1998; Walter et al. 2006; Münn et al. 2006; Wooller et al. 2004; Morgan and McGovern 2005; Delcamp et al. 2008). Grabens, en échelon faults, folds and thrusts are the characteristic spreading-related structures.

Intrusive complex emplacement phenomena have been studied separately from volcano gravitational spreading (e.g. Merle and Venderville 1992). A link between gravitational spreading and intrusion emplacement should exist, as suggested by van Bemmelen (1949), Borgia (1994) or Borgia and van Wyk de Vries (2003). According to Borgia (1994), the evolution of a volcanic edifice is divided into five stages that can be repeated, combined or absent: (1) a building phase, (2) is followed by a compressive phase due to an increase of volcanic load, (3) then a basal thrust occurred along a decollement, (4) followed by emplacement of an intrusive system and (5) finally, the intrusive complex spreads. To Borgia et al. (2000), dyke intrusion might contribute to the gravity spreading of the edifice by creating an additional forceful outward push. According to Merle and Vendeville (1992), vertical intrusion of a magma body generates gravity sliding along the

flank of the dome created by intrusion emplacement. In spreading, the intrusive complex induces extension within overlying brittle layer. Observed structures, such as those at Concepción, Nicaragua (Borgia and van Wyk de Vries 2003), Poas, Costa Rica (Borgia et al. 1990) or Etna (Borgia et al. 1992) should be a combination of both (1) volcano gravitational spreading and (2) intrusive complex emplacement and spreading.

The deformation related to small-scale intrusions has been also studied using Mogi, Okada and similar elastic models (e.g. Mogi 1958; Okubo and Watanabe 1989; Okada 1992; Fukushima et al. 2005). Such models are applicable for very small-scale elastic deformation relating to, for example, dyke emplacement, but are not applicable for large-scale nonelastic deformation, as considered here, where faulting and viscous flow occur. At the scale of our models, elastic deformation would only be in the order of less than a fraction of a millimetre. Because of this difference, we do not attempt any comparison with such small-magnitude elastic models, and any comparison would be meaningless.

Using scaled analogue models, we study the coupling of the two processes to assess the influence of intrusive complex emplacement in a spreading volcano. To emphasise the influence, we compared spreading sandbox models with and without intrusive complex emplacement. No such combined models have been done previously, and previous studies have either concentrated only on one process or the other. Finally, we compare the model results with various eroded and recent volcanic centres in both oceanic and continental contexts, and we especially focused in on La Réunion Island where the effect of intrusive complex emplacement and spreading interacts with gravitational spreading of the volcano.

Modelling

Experimental setup

We study two types of models, one with a basal ductile substratum diameter smaller than the volcanic edifice (type I) and the other with a diameter of ductile basal layer greater than the volcano (type II; Fig. 1). The first situation simulates a volcano with a basal ductile layer included in the edifice. Such a situation can be analogous to an oceanic volcano like La Réunion, Guadeloupe or Hawaii with within-edifice pelagic and detrital low strength layers (Oehler et al. 2005), or any volcano that has grown with weak inner layers (e.g. heavily weathered rocks). The second type of model represents a volcano built directly onto a ductile substratum layer, as it is generally the case for subaerial volcanoes or oceanic volcanoes on thick pelagic sediments.
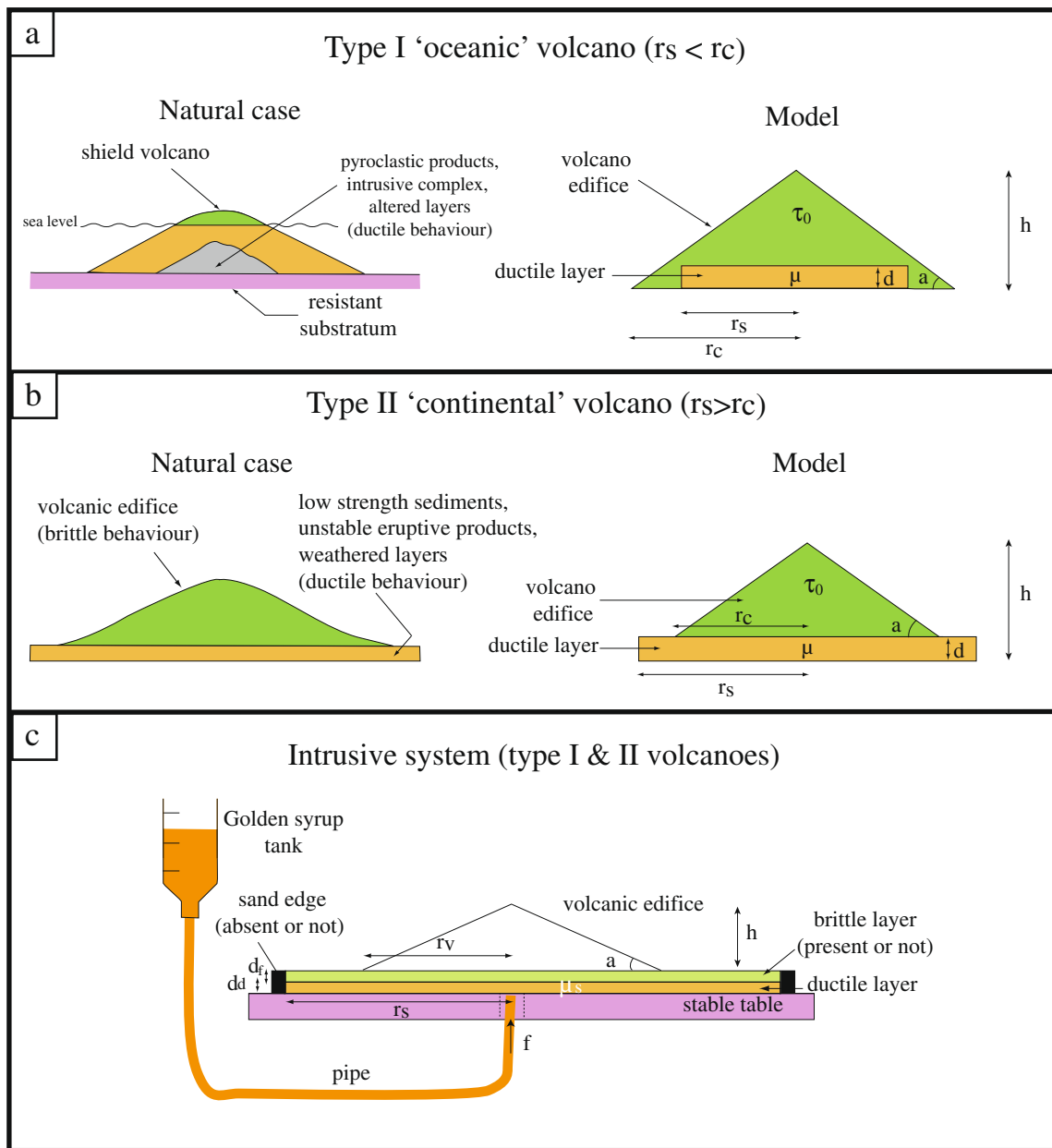
Fig. 1 Experimental setup. Two types of models have been tested: **a** type I 'oceanic' model, where the radius of the edifice is greater than the radius of ductile layer and **b** type II 'continental' model, where the radius of the volcano is smaller than the substratum; **c** Sketch of the experimental setup for intrusive models

The model is constructed on a flat rigid base in which a hole has been drilled. This aperture is connected by a pipe to a reservoir containing Golden syrup as a magma analogue (Mathieu et al. 2008). Emplacement of the analogue intrusive complex is generated by overpressure, as the reservoir can be raised above the experimental table. After the experiments, models are frozen at −18°C to preserve the form of the intrusive complex shape. Photographs of the models were taken at even time steps, allowing 2D horizontal deformation to be tracked and structure development to be followed. On some models, three cameras were used for full 3D photogrammetry.

Scaling and dimensionless analysis

Scaling assures the necessary conditions for maintaining the same geometric, time and force ratios between models and natural cases (Hubbert 1937; Ramberg 1981; Middleton and Wilcock 1994). Viscosity, density, cohesion and some other parameters are well scaled from previous similar experiments without intrusion (Merle and Borgia 1996;

Oehler et al. 2005; Walter et al. 2006). The scaling here follows closely to such previous studies (Table 1).

Length scale (l*) is 5.8×10^{-5}, density scale ρ*) is 0.57 and gravity scale (g*) is 1. The result of the following equation provides the stress and cohesion scale (σ*) that is thus about 10^{-5}:

$$l^* \times \rho^* \times g^* = \sigma^* \quad (1)$$

Using this, our model sand–plaster mix, which has a cohesion of about 100 Pa (it varies between 66 and 336 Pa), is the equivalent to a rock with a cohesion of about 10^7 Pa. Time scale (t*) is obtained from velocity information. We prefer to use velocity (u) rather than the previously used 'time of deformation' (Merle and Borgia 1996) as this latter parameter is hard to determine in nature and in the experiments. Characteristic flank displacement rates in the models are about 10^{-6} ms^{-1}, and we equate these to natural rates of about 10^{-10} ms^{-1} (equivalent to 1 cm per year). Thus, the velocity scale is 10^4. Using the length scale, the time scale can be extracted from the velocity scale:

$$l^*/u^* = t^* \quad (2)$$

Thus, the time scale (t*) is about 2×10^{-9}. The viscosity scale is obtained from the stress and time scales

$$\mu^* = \sigma^* t^* \quad (3)$$

The viscosity scale is thus 7×10^{-14}, which is equivalent to a substratum of $10^{17–18}$ Pa s and an intrusive complex viscosity of $10^{13–14}$ Pa s The substrata values are coherent with those used by other studies (Merle and Borgia 1996; Cecchi 2003), and the intrusive values are coherent with a viscosity expected for a semi-solidified magma body (e.g. Holohan et al. 2008). Consequently, the intrusive complex, composed of crystal-poor magma, crustal mush, cumulates

and partially solidified magma, is considered as one mechanically coherent unit (Hill and Zucca 1987; Okubo et al. 1997; Kauahikaua et al. 2000). Note that additional low-viscosity intrusions that may rise from the intrusive complex (i.e. dykes) are not and cannot be modelled here.

Viscosity of strata and magmatic bodies estimates may vary by several orders of magnitude (e.g. Murase and McBirney 1973; Marsh 1981; Rosenberg 2001). Both viscous intrusion and substrata behave as ductile material and are thus likely to deform in the same manner, but with different rates, over a large range of viscosity values. Consequently, the unknown natural values will unlikely affect the structural geometry observed, but will affect the rates of deformation.

Dimensionless numbers

Once the basic scaling is completed, the parameters can be cast into dimensionless numbers to study quantifiable elements of the model such as geometric parameters or fault density (Hubbert 1937; Ramberg 1981; Middleton and Wilcock 1994).

There are a large number of parameters, but as many of these are held constant, or do not change, they can be removed from the dimensionless analysis. For example, intrusion viscosity and diameter of feeding pipe stay constant. Previous experiments (Cecchi 2003; Delcamp et al. 2008) showed that substrata viscosity variation influences velocity, but not the type or geometry of the observed deformation. This parameter is therefore not included in the dimensional analysis. However, a scaled intrusion velocity can still be extracted and can be used for comparisons. The number of constant parameters allows a reduction of the number of variables to six, expressed with the dimensions of length and time (Table 2).

Table 1 Basic representative scaling parameters used, values for models and nature with their ratios

Parameters	Units	Model	Nature	Ratio (*)
Length (l)	m	0.07	1,200	5.8×10^{-5}
Density (ρ)	kg m^{-3}	1,500	2,600	0.57
Gravity (g)	m s^{-2}	9.81	9.81	1
Stress (σ)=l×ρ×g	kg m^{-1} s^{-2}	100	3×10^7	3.4×10^{-6}
Velocity (u)	m s^{-1}	8×10^{-6}	3×10^{-10}	2.7×10^4
Time (t)=l/u	s	1 min	900 years	2×10^{-9}
Viscosity substrata (μ)	kg m^{-1} s^{-1}	10,000	1.4×10^{17}	7×10^{-14}
Viscosity intrusion (μ)	kg m^{-1} s^{-1}	3	4×10^{14}	7×10^{-14}
Intrusion flux (f)	m^3 s^{-1}	2×10^{-8}	2.2×10^{-4}	9×10^{-5}
Dim. equivalence	μ / σ t=1		l/u t=1	

Note that the basic three parameters, length, density and gravity, provide the values for scaling for the three dimensions length, mass and time. Stress (and cohesion) are defined by the product, l×ρ×g. Velocity is estimated from models and nature, and time scaling is obtained from velocity and length. The scaling is verified by the dimensionless equivalence, μ / σ t=l/u t

Table 2 Significant model variables, given with the value ranges and their equivalents in nature. Π−Number description with model and equivalent natural ranges, and their ratios

Parameters	Definition	Models	Nature	Dimensions
h	Volcano height	0.01–0.07	170–1,200	m
r_v	Volcano radius	0.12–0.17	2,000–2,900	m
d_d	Thickness of ductile layer	0.006–0.032	100–500	m
d_f	Thickness of brittle layer	0–0.032	0–500	m
u	Displacement velocity	1.4×10^{-6}–8.7×10^{-6}	5×10^{-11}–3×10^{-10}	m s^{-1}
f	Intrusion flux	3×10^{-9}–2×10^{-8}	3.3×10^{-5}–2.2×10^{-4}	m^3 s^{-1}
μ_I	Intrusion complex bulk viscosity	3–6	10^{14}	Pa s
				Ratio M/N
Π_1	Height/radius of volcano	0.07–0.52	0.05–0.6	~1
Π_2	Volcano height/substratum thickness	1.31–8.33	1.17–12	~1
Π_3	Brittle layer/ductile layer thickness	0–4.33	0–5	~1
Π_4	Spreading force/intrusion flux	0.08–1.14	0.04–10.9	~1

Using the Π-Buckingham theorem (e.g. Middleton and Wilcock 1994), four dimensionless numbers can be established. Π1 is the ratio of volcano height to its radius. The volcano height for type I models includes the thickness of ductile substratum that constitutes a part of the edifice (i.e. ductile layer is included within the volcano edifice). The tangent of this number corresponds to the volcano slope.

$$\Pi1 = \frac{\text{volcano height}}{\text{volcano radius}} = \frac{h}{r_v} \quad (6)$$

Π2 is the ratio of the volcano height to the substrata thickness,

$$\Pi2 = \frac{\text{volcano height}}{\text{thickness of substrata (brittle + ductile)}} = \frac{h}{d_f + d_d} \quad (7)$$

Π3 is the ratio between the brittle layer and the ductile layer thicknesses. For type I models, the brittle layer is absent and Π3 can thus not be defined. For type II models, Π3 can vary from zero to infinity.

$$\Pi3 = \frac{\text{thickness of brittle substrata}}{\text{thickness of ductile substrata}} = \frac{d_f}{d_d} \quad (8)$$

Π4 aims to constrain the influence of both the intrusive flux and the displacement velocity on the deformation.

$$\Pi4 = \frac{\text{spreading force}}{\text{intrusive flux}} = \frac{u \times h \times (d_d + d_f)}{f} \quad (9)$$

The first three numbers are predefined by the experimental setup, while Π4 is a consequence of the input parameters and the system reaction as u (deformation velocity) is not fixed or constrained during the experiment. All values may vary with time according to the deformation of the model. Other variables that have no dimensions can be added, such as the number or density of faults and number of grabens.

Materials

Brittle layer

Pure sand has been used often for models of brittle volcanic rocks (e.g. Merle and Borgia 1996). In this study, sand is mixed with 10% plaster to increase the cohesion to a value scaled with natural rocks (Donnadieu 2000). Furthermore, this also allows much more structural detail to appear at the surface.

Ductile layer

Silicone is the ductile rock analogue material, referred to as low strength layers (LSLs in Oehler et al. 2005) that can constitute part of the volcano and/or the volcanic basement. Viscosities of these natural layers are still poorly known, but are estimated at 10^{18} Pa s by Carena et al. (2000) and at 10^{14-15} Pa s by Arnaud (2005). The range of viscosities will influence the displacement velocities, but not the style of deformation (Merle and Borgia 1996). We chose thus an intermediary value of 10^{17} Pa s. The silicone viscosity here varies between 10^4 (clean silicone: SGM 36, Dow Corning) and 8.10^4 Pa s (pure silicone mixed with a small quantity of sand).

Magma

Magma and intrusive complexes are generally much less viscous than the surrounding ductile rocks. Thus, we

introduce a viscosity contrast between intrusive complex and sediment layers. Golden syrup is a good analogue for magma (Mathieu et al. 2008; 2009). Viscosity varies between 3.5 Pa s at 25°C and 0.084 Pa s at 60°C. Room temperature varied between 20°C and 27°C during experiments corresponding to a variation of Golden syrup viscosity from about 5.9 to 3 Pa s.

Magma viscosities vary from 10 to 10^{18} Pa s depending on crystal content and melt composition. According to the scaling, Golden syrup represents here an intermediate value which can correspond to a crystal-rich magma, or can represent a bulk value for an entire intrusive complex (e.g. Murase and McBirney 1973; Marsh 1981; Rosenberg 2001).

Magma fluxes in nature are estimated from volumes emitted during eruptions, from estimated ages and edifice volumes, or from deformation and degassing data (Wadge 1982; McNight and Williams 1997; Hasenaka and Carmichael 1985; Beauducel et al. 2000; Wicks et al. 2002). Approximate values vary from 0.01 to 0.5 $m^3 s^{-1}$. Fluxes in models (without eruption) are 10^{-9}–10^{-8} $m^3 s^{-1}$ that scale to 10^{-4}–10^{-3} $m^3 s^{-1}$ in nature. Thus, models correspond here to 1/100 of the estimated natural fluxes. These values can be coherent if magma storage does not correspond to the total amount of magma flux in the system, some being lost by eruption (a situation that occurs when the intrusive flux is increased in the models) or by crystallisation. Furthermore, note that we study here the growth of an intrusive complex over a long period, when flux is lower than during short eruptive episodes, i.e. when most flux estimates have been calculated.

Results

Analogue model description

The parameters we changed and considered were the volcano slope, the thickness of brittle and ductile layers, and the intrusive flux. Three brackets of slope values were tested: ~10°, ~20° and ~30°. It is difficult to construct a cone with an exact slope, and the angle of each cone was measured with a clinometer to obtain the true slope angle. The variation of Π1 values reflects the variation of the slope value. The thickness of the brittle and ductile layers is fixed at the start of the experiment, but as the slope, they vary with time. The intrusive flux was kept low to avoid the intrusive body appearing at the surface. The flux varies also with time.

In all the models, characteristic spreading structures were formed, i.e. grabens, folds (Borgia 1994; Merle and Borgia 1996; Borgia et al. 2000; Walter et al. 2006) and en échelon strike-slip faults (Delcamp et al. 2008). To describe the

models, we used cardinal points where the north corresponds to the top of the picture.

Type I internal ductile layer volcano

For type I model, steep cones of about 30° were characterised by intense faulting and fracturing. The structures formed a dense nearly radial network with certain sectors slumping out more rapidly than others.

For intermediate slope models (~20°) fewer structures formed. A single transverse graben was formed first and passed through the edifice centre and the intrusive complex location (Fig. 2a). Subsequent minor grabens were formed, as well as slumps at the model edge.

The deformation of the low-slope models (~10°) was concentrated around the intrusive complex, where a highly fractured uplift was observed. Small slumps and collapses were formed at the foot of the edifice as the edge spread out (Fig. 2b). Few or no grabens were formed in this case.

Type II volcano with substrata ductile layer

These models all evolved in a predictable pattern, with the early formation of flank grabens and summit fracturing and flattening (Fig. 2c, d). In models with thick brittle layers, strike-slip faults developed at the cone foot and were connected to graben extremities. These faults were propagating in the brittle layer. In the early stages, a subtle surface bulge with minor fracturing provided evidence of the intrusive complex growth within the spreading volcano. This bulge was rapidly transformed into a densely fractured depression. The bulging phase was not observed for experiments with a high spreading displacement velocity, for example for those with thin brittle layers.

In models without a brittle layer, many grabens formed within the cone. However, once a brittle layer was introduced, the number of grabens decreased. In fact, an increase of brittle layer thickness limits the formation of grabens (see "Dimensionless numbers" section). This effect was previously observed on gravitational spreading models (Delcamp et al. 2008). For models with a thick brittle layer, only a single graben was formed and traversed the edifice through its centre. Smaller grabens forming discrete spreading sectors developed from this central graben. An example of a typical model is J3 (Fig. 2c) that spreads initially towards the east from a single NNW–SSE transversal graben. Strike-slip displacements along the faults have been observed and were associated with the formation of en échelon fractures (zoom of the graben on Fig. 2c). The preferential spreading direction (eastward for the model J3 for example) was found to be due to model asymmetry, where the thickness of brittle layer varies slightly (Cecchi 2003).

Fig. 2 **a** L2 model (Π1=0.27). After 35 min; we observed the formation of an arcuate transversal graben going through the intrusion point; **b** L3 model (Π1=0.12) after 1 h and 5 min, significant horizontal deformation above the intrusion is seen by surface cracks and exhumation of underlying layering; **c** J3 experiment after 50 min (Π1=0.15 and Π3=4.33); **d** J1 model (Π1=0.17 and Π3=0) after 25 min; two centres of deformation are clearly visible, one organised around the intrusion point (in *grey*) and the other (in *black lines*) organised around the summit
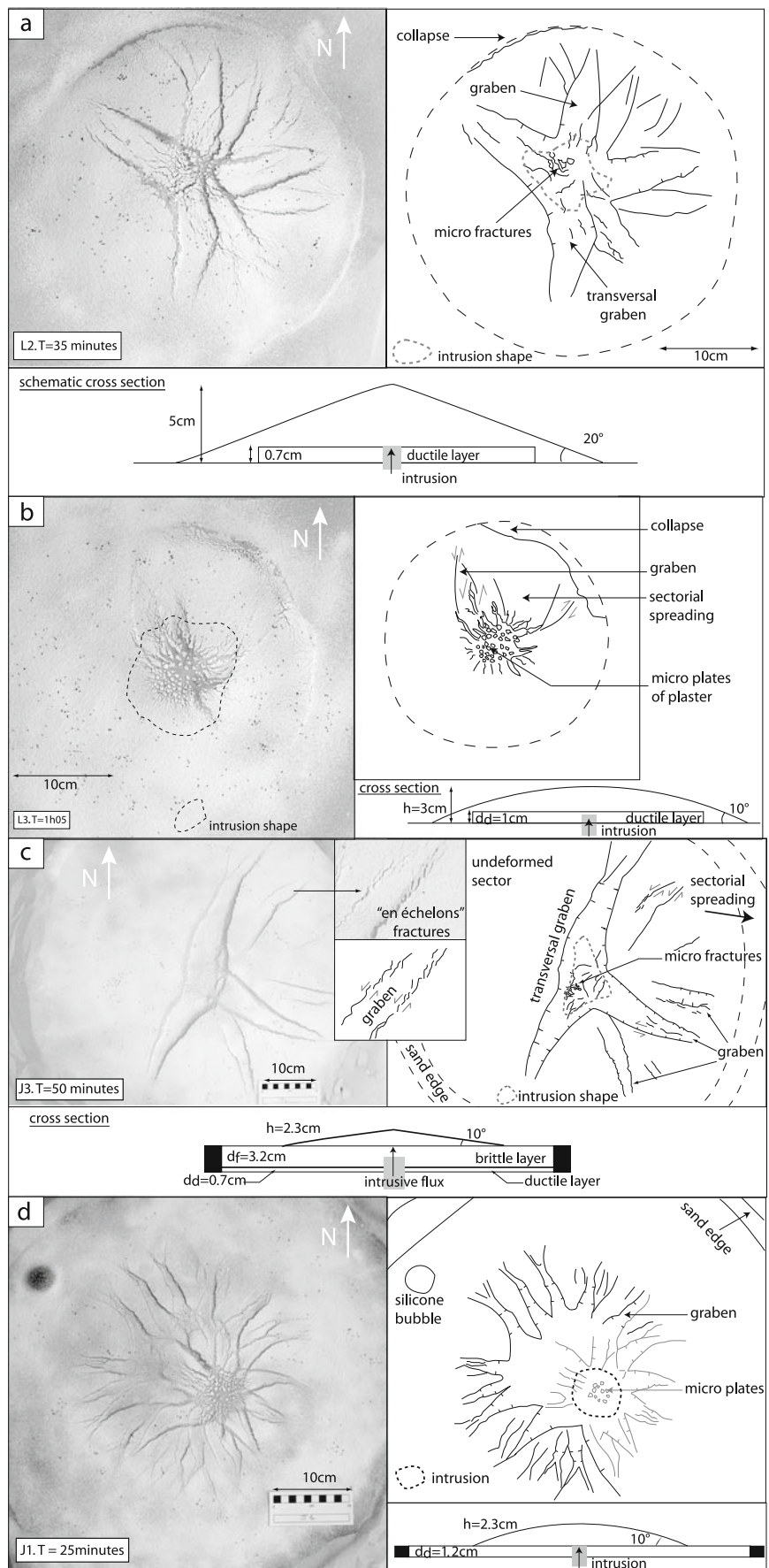
Thrusts and folds occasionally formed along the model border when the experiment was limited by a sand boundary. This even occurred when the boundary was set far from the model volcano (more than 50 cm). At such distances in nonintrusion experiments, no thrusting was observed. Thrusts and folds also appeared at the base of individual spreading sectors.

Dimensionless numbers analysis

We note that the number of graben increased with slope ($\Pi 1$) and the number of graben decreased with increasing thickness of brittle layer (represented by $\Pi 3$; Fig. 3a). For low $\Pi 3$ values, multiple graben formed, while a $\Pi 3 > 1.25$ allowed the formation of a single graben that traversed the edifice and passed above the intrusive complex. For larger $\Pi 3$ values (>3; Merle and Borgia 1996), spreading should be inhibited and no structures should form. Even above this limit, the experiments with intrusive complexes spread, leading to graben formation (experiments I5, J3 and K3, Table 3). However, for much higher $\Pi 3$ values, the intrusion propagated as a sill under the edifice and formed a bulge at the cone foot. A poorly defined graben was formed at the summit. During the experiments, it was possible to follow the sill propagation as a graben progressively formed above the sill.

In thin brittle layer models ($\Pi 3 < 0.52$), the volcano foot was surrounded by folds. For $\Pi 3 > 1$, no folds were observed and strike-slip faults radial to the cone were rather formed.

The $\Pi 4$ number, and thus displacement velocity and intrusive flux, did not play any role on the density of structures observed over the range studied. However, there is a linear relationship between $\Pi 4$ and $\Pi 1$ (Fig. 3b). The length of the intrusion is linked to $\Pi 3$ (Fig. 3c).

Morphology of the intrusions

Intrusive complexes were intruded from the feeder pipe into the ductile basement and then rose into the spreading cone. In all cases, they intruded and developed within the ductile level, attested by the thin silicone layer that enveloped the intrusive complex. Intrusive complex shapes could be classified into three principal morphologies:

1. The first type was characterised by a cylindrical base of variable height and diameter (Fig. 4). The summit could be flat or slightly bulged. The border of the intrusion was undulating and ridged. These small dyke-like, pointed intrusion features were linked to substrata silicone ridges, which formed at the intersection between the conjugate faults that formed individual graben. This first type of intrusive complex shape
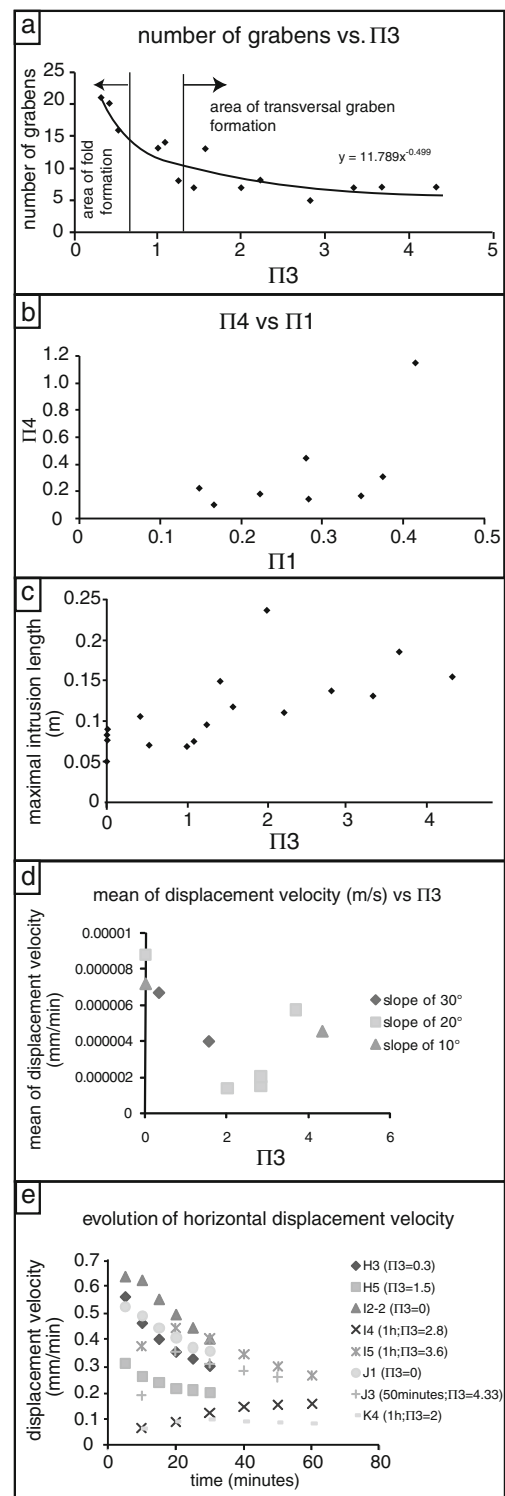
Fig. 3 Graphs of parameters varying in the models: **a** number of grabens vs. $\Pi 3$ (brittle/ductile thickness ratio); **b** $\Pi 4$ (spreading force/intrusive flux) vs. $\Pi 1$ (volcano slope); **c** maximum length of the intrusion (in metres) vs. $\Pi 3$; **d** average of displacement velocity (m s^{-1}) vs. $\Pi 3$; **e** evolution of the horizontal displacement velocity (mm min^{-1}) vs. time

occurred when the basal ductile layer was covered by a very thin layer of brittle material ($0 < \Pi 3 < 1$). The

Table 3 Description of the experiments

	Angle	h (m)	d_d (m)	d_f (m)	r_v (m)	r_s (m)	Other information	Number of structures
H1	30°	0.057	0.008	0	0.12	0.51	i.f the most rapid/c.s	28
H2	30°	0.0572	0.0078	0	0.15	0.3	c.s	28
H3	30°	0.0497	0.0078	0.0025	0.12	0.28	b.d.s	21
H4	30°	0.0572	0.0078	0	0.1325	0.27	e.s/b.d.s	28
H5	30°	0.05	0.0064	0.01	0.14	0.27	e.s/b.d.s	13
H3sp	30°	0.0565	0.006	0.0025	0.135	0.27	e.s/c.s	
H5sp	30°	0.07	0.007	0.01	0.14	0.25	e.s/c.s	
I1-1	20°	0.038	0.009	0	0.15	0.28	e.s/edifice without cohesion/b.d.s	24
I1-2	20°	0.0536	0.0104	0	0.145	0.28	e.s/edifice without cohesion/b.d.s	25
I2-1	20°	0.0498	0.0092	0	0.1325	0.28	e.s/cohesive edifice/b.d.s	28
I2-2	20°	0.0542	0.0088	0	0.145	0.28	e.s/cohesive edifice/b.d.s	21
Iannexe2	20°	0.0395	0.0105	0	0.135	0.29	e.s/b.d.s	19
Iannexe3	20°	0.0304	0.0096	0.005	0.13	0.28	e.s/b.d.s	16
Iannexe4	20°	0.0318	0.0102	0.011	0.145	0.29	e.s/b.d.s	14
I3	20°	0.037	0.008	0.01	0.13	0.27	e.s/b.d.s	8
I4	20°	0.0395	0.008	0.0225	0.14	0.29	e.s/b.d.s	5
I5	20°	0.035	0.0075	0.0275	0.125	0.25	e.s/b.d.s	7
J1	10°	0.023	0.012	0	0.1375	0.3	e.s/b.d.s	21
J2	10°	0.015	0.01	0.01	0.13	0.3	e.s/b.d.s	13
J3	10°	0.023	0.0075	0.0325	0.155	0.27	e.s/b.d.s	7
K1	20°	0.04525	0.00775	0	0.125	0.28	e.s/i.f decreased/ b.d.s	18
K2	20°	0.036	0.009	0.02	0.125	0.27	e.s/i.f<i.f K1/ b.d.s	8
K3	10°	0.01	0.0075	0.025	0.1375	0.29	e.s/i.f=i.f K2/ b.d.s	7
K4	20°	0.03	0.01	0.02	0.135	0.28	e.s/i.f<i.f K2/b.d.s	7
L1	30°	0.069	0.011	0	0.155	0.125	b.d.s	22
L2	20°	0.043	0.007	0	0.155	0.125	b.d.s	16
L3	10°	0.02	0.01	0	0.165	0.125	b.d.s	3
L4	10°	0.0225	0.0095	0	0.16	0.125	b.d.s	9
M	20°	0.016	0.024	0	0.15	0.6275	e.s/i.f=i.f K4/ b.d.s	33
M2	20°	0.032	0.032	0	0.17	0.6315	e.s/ b.d.s	14
I	30°	0.075	0	0.018	0.125	0.435	No brittle substratum, no volcano	

In bold, type I volcano; in italic, type II volcano

Angle model slope, *h* model height, d_d thickness of ductile layer, d_f thickness of brittle layer, r_v volcano radius, r_s basal layer radius. *c.s* clean silicone, *i.f* intrusion flux, *b.d.s* silicone mixed with sand, *e.s* sand edge border

thicker the brittle layer, the fewer ridges formed, corresponding to the decrease in the number of graben. The ridges were also larger. Type I volcanoes (internal ductile layer) with a slope of 20° and 30° also developed such intrusive complex morphology (L1 and L2 experiments; Table 3).

2. The second type of intrusive complex morphology occurred for models covered with a thin brittle layer ($1 < \Pi 3 < 1.56$). The intrusion base was more spread and flattened, and the top was bulged (Fig. 5a). Crests are visible on the outer parts and are linked to the traces of fault-related silicone ridges and to the graben in which the intrusive complex was emplaced.

3. The third type formed when the brittle layer was thick ($2.22 < \Pi 3 < 4.33$): intrusive complexes were principally developed in two opposite directions and formed fat, short intrusions connected to silicone ridges (Fig. 5b). For thicker brittle layers, the intrusion spread as a sill only and eventually rose on a radial dyke-like intrusion to erupt at the cone foot.

The three main morphologies represent end-members and general cases. In detail, each intrusive body displayed slight variations, and occasionally, morphology could be very different. For example, J1 model ($\Pi 1 = 0.17$ and $\Pi 3 = 0$) allowed the formation of an almost perfect cylinder.

Fig. 4 Results from model I1-2 ($\Pi 1=0.37$ and $\Pi 3=0$): **a** picture and sketch of exhumed silicone substrata layer showing central intrusion and ridges associated with grabens. The close relationship between the intrusion fingers and the ridges is clearly visible; **b** the intrusion extracted after freezing, in two views; **c** cross-sectional sketch of the model setup
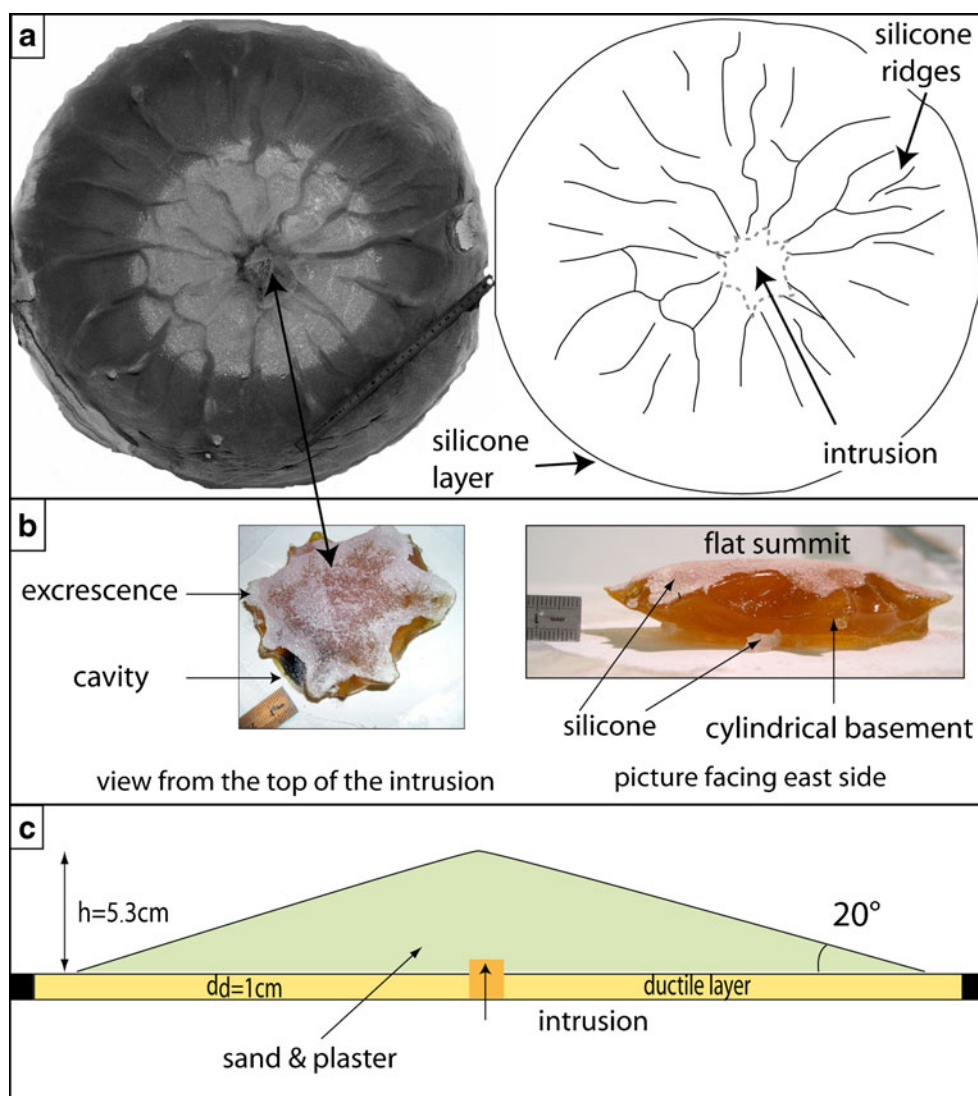
All the intrusive complexes mimic the structures observed at the surface. Ridges, dykes and undulations corresponded to the graben formed at the surface. For example, for the L3 model, the intrusive body reproduced the horseshoe-shaped graben (Fig. 2b).

Displacement

Different intrusive rates were applied to models of same geometry. For example, the models H1 and H2 displayed the same geometry, but H1 had a higher flux (Table 3). In this case, the displacement rate was higher for H1. In H1, unlike H2, no clear structural pattern occurred and the model was rather characterised by disorganised fracturing. Moreover, the intrusive complex pierced the surface.

A correlation between $\Pi 3$ and the displacement velocity exists, where higher $\Pi 3$ induces lower displacement velocity (Fig. 3d). Models with $\Pi 3>2$ show an acceleration phase that becomes more pronounced with greater brittle

layer thickness (Fig. 3e). After this acceleration, velocities generally decreased. We note that I4 model shows acceleration, but velocity does not diminish afterwards.

2D displacement velocity fields

Using pictures, horizontal displacement fields were calculated over sequential time steps (Fig. 6). For models with no intrusion, greater $\Pi 1$ and $\Pi 2$ are always associated with faster spreading, and the spreading rate decreases as the volcano height is reduced. The first result to note is that displacement fields obtained for gravitational spreading alone and for models associated with intrusive complex emplacement clearly differ. The horizontal displacement fields were more variable for models with an intrusive complex (Fig. 6a–c) than without (i.e. classic spreading cone, Fig. 6d).

In addition, displacement occurred further out from the centre. Above the intrusive body, the models displayed a
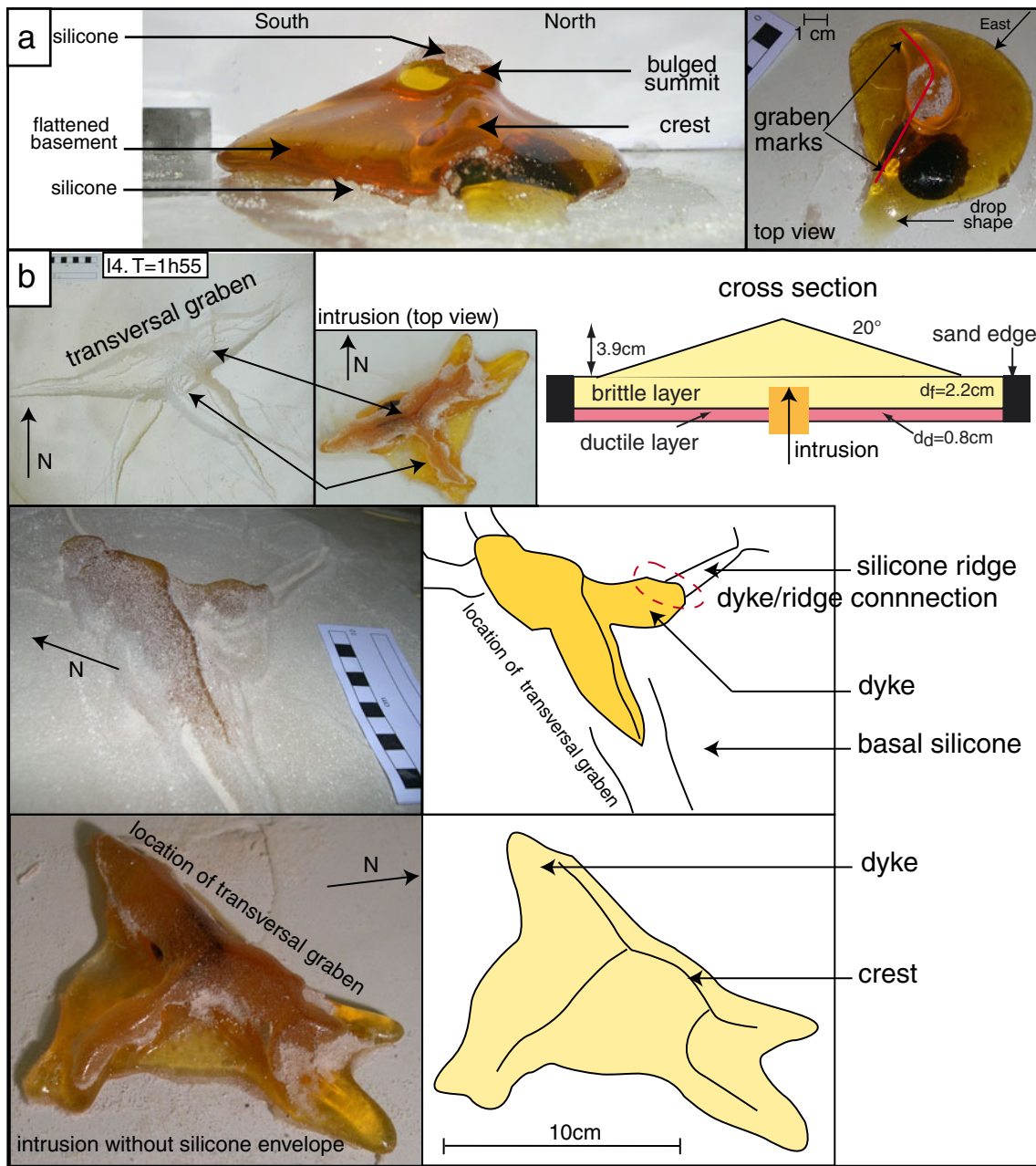
Fig. 5 Details of intrusion shapes and relationships with substrata: **a** model I3 (Π1=0.28 and Π3=1.25); intrusion shape after freezing, note the upper bulge and the flatter base with ridges; **b** I4 model (Π1= 0.28 and Π3=2.81); picture at the *top* is the model after 1 h and 55 min. Photo in the *middle* and associated sketch correspond to exhumed frozen model. On the *bottom* photo, the thin silicone layer that covers the frozen intrusion has been removed to show clearly the intrusion shape. Dykes were formed and propagated in the silicone ridges below the grabens

greater horizontal component than for models without intrusion, and the maximum displacement on the volcano flanks extended further out.

A model with an intrusive complex that is offset from the volcano summit produces two centres of deformation. For example, visual inspection of the J1 model shows two areas of deformation around which are organised two systems of grabens (Fig. 2d). These two centres are also visible on horizontal displacement field maps (Fig. 6a).

When spreading is restricted to one sector, such as in model J3 (Fig. 6b), the horizontal displacement field is clearly concentrated on this spreading sector (Fig. 2c), in which the intrusive complex develops.

3D displacement velocity fields

We used stereophotogrammetry to obtain horizontal and vertical velocity components. Three cameras and the
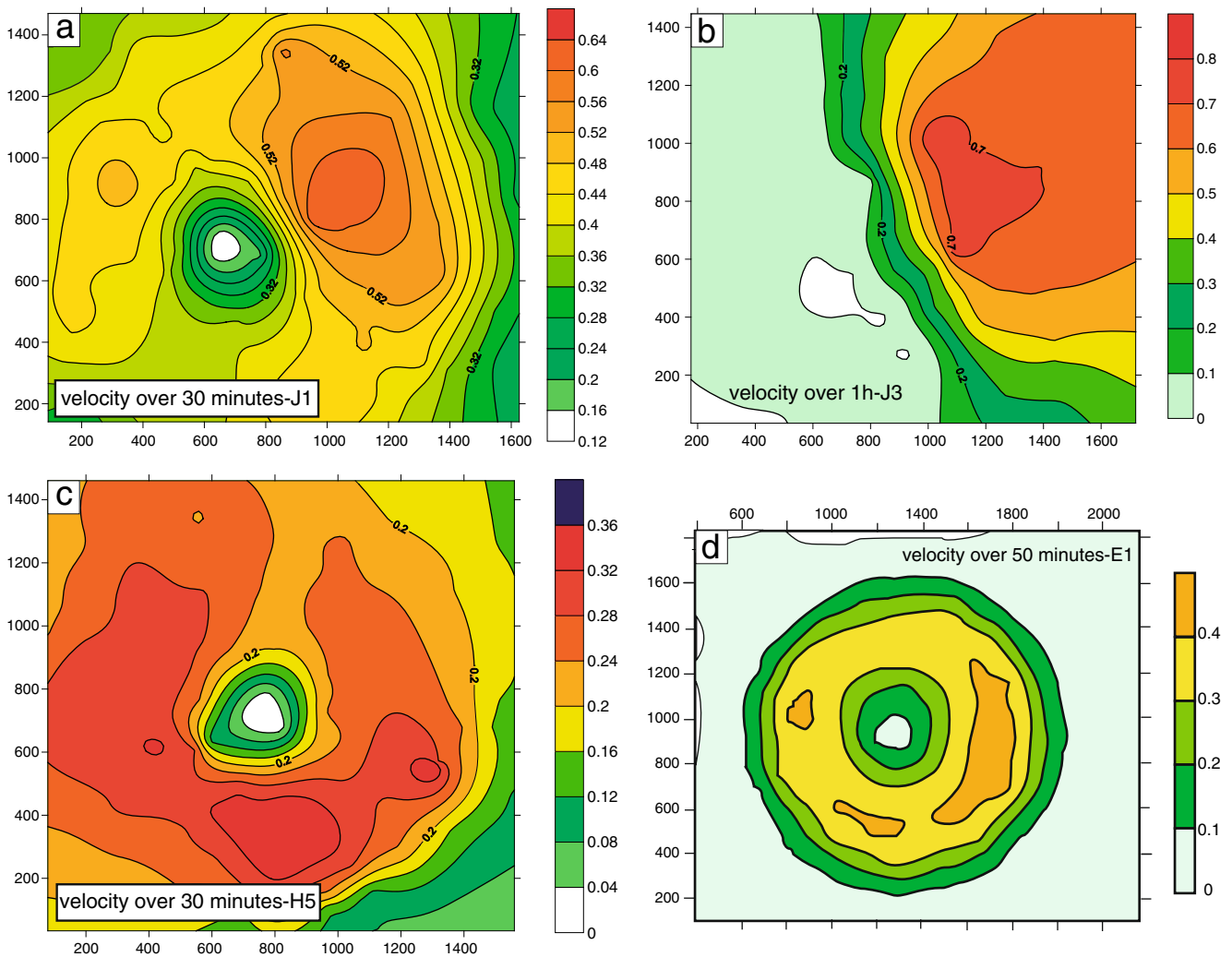
Fig. 6 Horizontal velocity displacement field maps: **a** map of J1 model (Π1=0.17 and Π3=0) determined over 30 min (model in Fig. 2d); **b** map for J3 model (Π1=0.15 and Π3=4.33) over 1 h; **c** H5 model (Π1=0.36 and Π3=1.56) over 30 min (model in Fig. 2c); **d** map of spreading model with no intrusion for comparison

geometry were calibrated with Visual Measurement System (VMS; Robson and Shortis 2004, http://www.geomsoft. com). Points were manually chosen in VMS to be sure that there was low initial error. Point positions were tracked on each image. Then, the coordinates (x, y, z) were obtained using a script written in Matlab. The results are synthesised in Fig. 7.

For one model, we obtain three figures. The X-axis corresponds to time from the start of the experiment. The Y-axis represents radial distance from the centre of the model, so zero is the cone summit and the greatest number is the model edge. Associated colours give displacement magnitude for each distance and time. Dark blue areas are those with no data. The first figure is the variation of velocity magnitude (horizontal and vertical component) with time (X-axis). The second figure is the variation of the horizontal velocity component with time, and the third

figure is the variation of the vertical velocity component with time.

Figure 7a is a model with an initial slope of 30° and no brittle substrata. Velocity reaches a maximum and is concentrated at the centre, but the value varies with time. The horizontal component is highest between 6 and 10 cm. We note an increase of the velocity at 4 cm from the centre between 14 and 20 min and a maximum at the end of the experiment corresponding to the intrusive complex rising close to the surface. Vertical velocity reaches a maximum at the centre and decreases outwards. However, we observe an increase of velocity towards the end, which again corresponds to the approach of Golden syrup towards the surface.

Figure 7b corresponds to a model with the same geometry to that of the model in Fig. 7a, with an initial slope of 30°, but without any intrusive complex, i.e. where
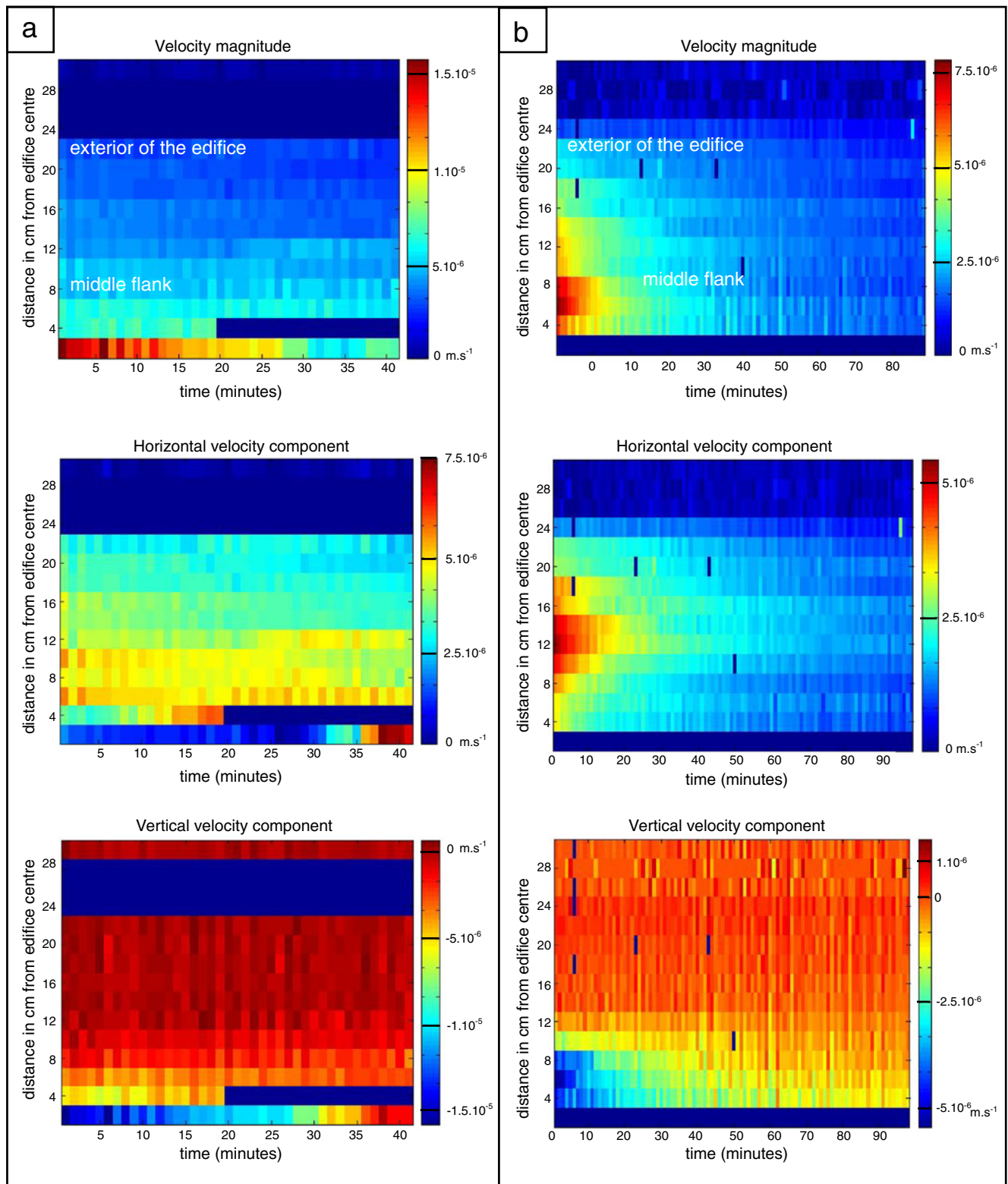
Fig. 7 3D evolution of displacement velocities for spreading only and spreading with intrusion models: **a** with an intrusion and an initial slope of 30°; **b** without an intrusion and an initial slope of 30°. *Y*-axis is the radial distance from the centre of the model. *X*-axis is the time, shading gives the velocity magnitude. At the *top*, evolution of total velocity magnitude in time; in the *middle*, evolution of the horizontal component of velocity during time; at the *bottom*, evolution of the vertical component of velocity during time

only gravity spreading occurs. In this case, velocity magnitude decreases from the centre outwards and we observe a peak at 6 cm, over the mid-flank of the edifice. Areas with lower displacement rates reach a constant velocity sooner than areas with initial high displacement rates. Maximum of velocity does not occur at the same location for the x and y components. Vertical velocity reaches a maximum (downwards) at the centre and decreases outwards, while horizontal velocity reaches a maximum (outwards) at the flank (12 cm).

Interpretations of the analogue model results

Role of the brittle substrata

The thickness of substrata brittle layer was found to be the most important factor that influences the number of structures formed, the intrusive complex morphology and the displacement velocity. In general, for spreading volcano models, increasing the brittle substrata layer (increasing Π3) restructures the stress field and diminishes the number of grabens (Merle and Borgia 1996; Delcamp et al. 2008). Previously, we noted a relationship between the length of the intrusion and Π3 (Fig. 3c). Intrusive complexes were emplaced and developed within the grabens. Consequently, in models where few grabens were formed, a larger relative volume of Golden syrup was intruded below each graben. This allowed the intrusive complex to develop fewer but longer branches. In addition, fewer numbers of grabens mean that fewer structures can accommodate the deformation. The displacements along these structures are thus higher allowing asymmetry to develop. This produces sector spreading. The spreading sectors formed in the part of the model where the brittle substratum is thinner.

On the J3 model, gravitational spreading alone was totally inhibited by a thick brittle substrata (Π3=4.33); however, grabens and volcanic rift zones were still formed (Fig. 2c). This model had structures organised around a slight thickness variation in the brittle substrata. Consequently, a slight asymmetry in the model favours an asymmetric development of the intrusive complex that may have concentrated stresses enough to generate the limited intrusion-related spreading.

Role of the intrusive complex

The intrusive complex emplacement does not create new types of structures compared to those formed in a spreading volcano. At low Π3 values when spreading is already occurring, intrusion and substrata contribute together to the formation of the structures, and the two deformation fields are merged.

When the spreading was supposedly inhibited by the presence of a thick brittle layer of constant thickness (i.e. Π3>3), a poorly defined graben or a set of fractures formed at the summit, i.e. above the intrusive body. The rest of the deformation was characterised by the propagation of the complex as a sill below the edifice. This shows that intrusive complexes can favour a moderate localised spreading if the volcano is initially in a stability domain. Obviously, for a very thick brittle cover, spreading would not be triggered at all. In these cases, the intrusion formed a sill-like body in the ductile layer. Thus, the intrusive complex spread, but not the overlying volcano. No precise limit was found between spreading induced by intrusive complex emplacement and sill formation, and the change-over is probably very sensitive to small variabilities in model construction.

In intrusion models, even when the model boundary was set up far from the edifice itself, the formation of thrusts and folds along the edge occurred. At such distances, in no-intrusion gravitational spreading experiments, no thrusting was observed. Thus, with intrusion the deformation field extends further out. This effect is also seen in the deformation field on Fig. 7, where in 7a there is deformation registered up to the model edge, but not in 7b, the nonintrusion case.

Two different systems might be responsible for gravity spreading, the first due to a basal ductile layer under the volcano and the second due to the growth and the spreading of the intrusive complex as suggested by e.g. van Bemmelen (1949), Borgia (1994), Borgia et al. (2000), Borgia and van Wyk de Vries (2003).

In a few experiments, such as model J1 (Fig. 2d), we observe two distinguishable systems of graben. Thus, two deformation complexes may exist: one due to spreading of silicone layer and the second due to intrusive complex emplacement.

Displacement velocity and intrusive flux

We previously observed a linear relationship between Π4 and Π1 (Fig. 3b) that can be due to a combined effect: the steeper the cone, the faster the system spreads on the ductile layer, and consequently, the steeper the cone, the faster the intrusion may spread. This suggests that the cone may slide along the intrusion. A similar effect was found for deep intrusions into volcanoes with decollements by Mathieu and van Wyk de Vries (2009), where the intrusion domes the substrate, causing outwards sliding.

For the same geometry, a higher intrusive flux induces a disorganised structural pattern, and there is higher displacement velocity (see for example models H1 and H2). Consequently, intrusive flux influenced deformation style.

In comparing Fig. 7a with 7b, we see clearly that adding the intrusion disturbs significantly the displacement field, which is concentrated around the intrusion. Furthermore, deformation extends further from the edifice and is more prolonged as also observed in the 2D horizontal displacement measurements.

Shape and evolution of the intrusion during spreading

The intrusive complex develops vertically and horizontally depending on the surrounding substrata and edifice. The extreme case is a model with no volcano or brittle layer: experiment I (see Table 3) consists of an intrusion in a silicone layer without sand cover. Deformation is characterised by a bulge stage rapidly followed by a spreading phase. The intrusion does not pierce the silicone, and its summit flattens as its diameter increases. In the main set of models, intrusive complex morphologies also show these bulging and spreading stages (Figs. 4 and 5) with the presence of summit bump and crests (bulging phase), as well as long intrusive branches and lateral bulge formation (spreading phase). The intrusive complex is thus affected by vertical and horizontal expansion. The bulging stage is followed by the spreading stage, though there may be a continuous competition between gravity spreading and Golden syrup push, as suggested by the velocity fluctuations.

Rapid outward horizontal deformation is observed above the rising intrusive complex; at this location, the fine plaster model surface is highly fragmented allowing the exposure of the inner cone layers. Displacement field patterns show this rapid spreading, for example for the J1 model (Fig. 6a).

The above results are in accord with the hypothesis of Borgia (1994) where the intrusive complex can spread and also highlights the important link between gravity spreading and the intrusive complex. The fifth stage described by Borgia (1994), i.e. spreading of intrusive complex, occurred from the very beginning of the experiments. Consequently, some of the five stages described by Borgia (1994) could combine and operate at the same time.

Comparisons with natural cases

In this section, we concentrate on comparing the structures observed in the topography, in the field and by geophysics on La Réunion Island, as there is a clear link between major intrusive complexes and the structure of the island (Gailler and Lénat 2010; Michon and Saint-Ange 2008). Other interesting cases are presented elsewhere; for example, the Mull Central Complex in Scotland has been interpreted as a gravity sliding and uplifting intrusion that has deformed the surrounding substrata and volcanic rocks (Mathieu et al.

2008). The examples set out in Fig. 8 can also be interpreted in the light of the modelling. For example, the Ardnamurchan intrusion (Scotland) has small protuberances, linked to faults, and these features may be similar to the ridges seen in some of the analogue intrusions; a close look at the structure of the intrusion would be interesting to see if there is evidence of the intrusion growth and spreading (Fig. 8a). For the Concepción and Maderas volcanoes (Borgia and van Wyk de Vries 2003), where there is a clear spreading signature, the postulated intrusive complexes lie under the edifice; thus, on geological evidence alone, there is no clear way of distinguishing gravitational spreading along from intrusion-related spreading (Fig. 8b). However, there are two lines of evidence that suggest that interplay has been operating: (1) The graben system on Maderas is slightly offset with respect to the central crater. This may be related to an offset intrusion. (2) On Concepción, Borgia and van Wyk de Vries (2003) report mudstones outcropping at up to 200 m above lake level, on the edifice flank. This may not be related solely to the folding related to the spreading of Concepcion, but may also be related to uplift due to the intrusive complex. For both of these cases, dedicated deformation monitoring and gravity modelling might provide confirmation of the interaction between the intrusive complex and the edifice spreading.

Piton des Neiges

La Réunion Island is composed of an active edifice, Piton de la Fournaise, by a dormant edifice, Piton des Neiges, and a mainly buried volcano, Les Alizés (Lénat et al. 2001). In the topography of the island, best viewed on a shaded relief digital elevation model, there is a clear star or flower-shaped pattern of escarpments and valleys (locally called Cirques) that look similar to the grabens observed during our experiments (Fig. 9a, b). This pattern has been already suggested by Borgia et al. (2000) and van Wyk de Vries et al. (2001) to be a spreading related set of sector grabens. While the pattern appears clear in the topography, finding clear evidence in the field has been more difficult (e.g. van Wyk de Vries et al. 2001). Here, we report evidence from several field surveys in Cilaos Cirque and elsewhere. In the field, few faults are found, even with excellent outcrops and huge cliffs. However, the rocks forming the central part of Piton des Neiges contain severely fractured rock, where lavas are transformed to breccias (Fig. 10). The original fresh lavas and their associated breccias were already extensively fractured by emplacement and cooling mechanisms, and such densely fractured units do not favour the localisation of discrete faults as the preexisting fractures themselves take up significant amounts of strain (Lebas 2009). Thus, on La Réunion, diffuse shear zones made up
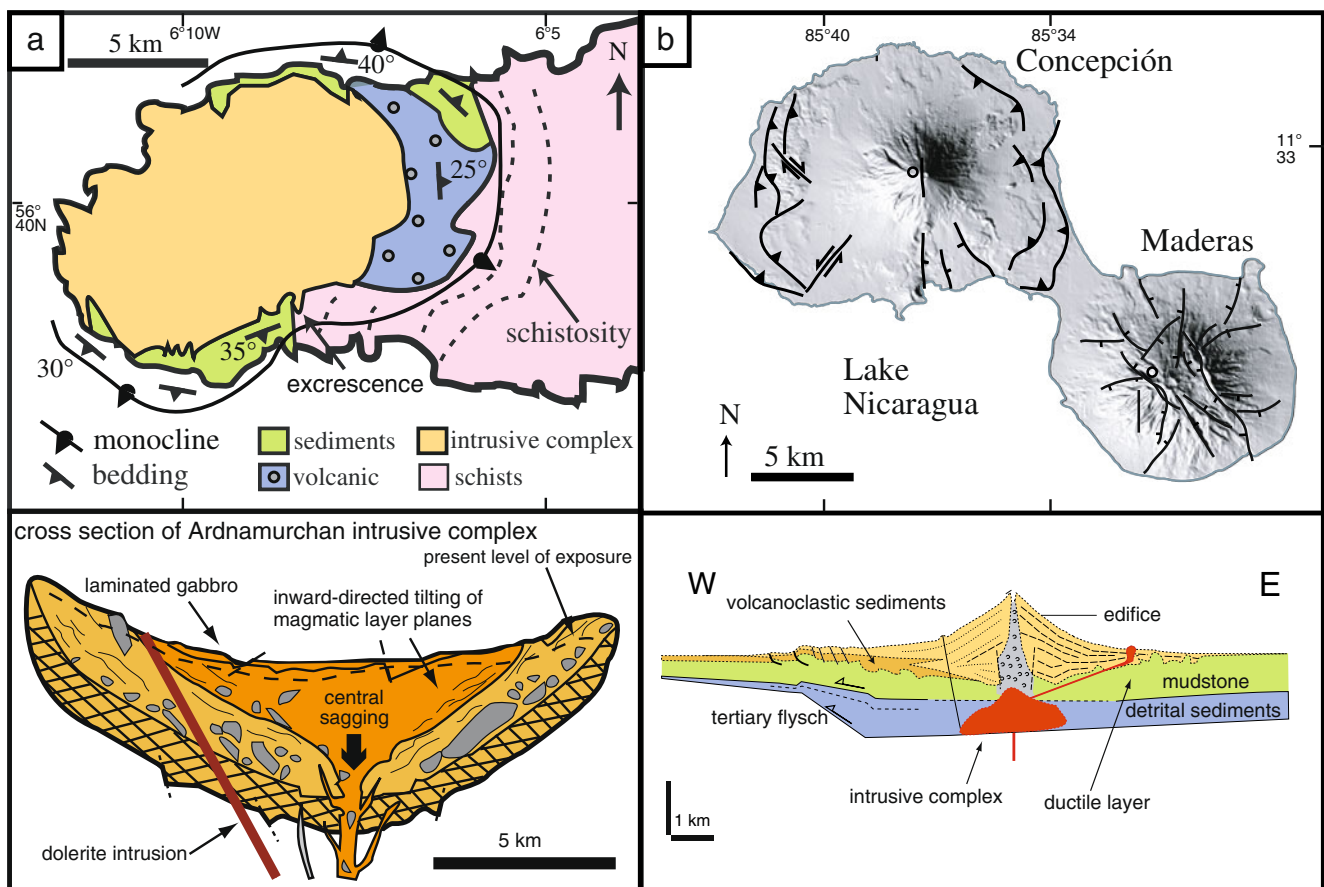
Fig. 8 a Tertiary intrusive complex of Ardnamurchan (Scotland), some thick finger-like protuberances from the main body are connected to strike-slip faults (cross section modified from O'Driscoll et al. 2006) b Shaded relief image and structural sketch of Concepción and Maderas volcanoes (Nicaragua). These two volcanoes have spread, or are spreading, and have probably well-developed intrusive complexes (Borgia and van Wyk de Vries 2003). Note that on Maderas, some grabens are significantly offset to the east of the actual summit crater, suggesting two centres of deformation, one gravity-controlled, and the other possibly intrusion-generated

of dense fracture networks are expected for any graben faults rather than localised fault planes (Figs. 10 and 11).

In outcrops that are located at about 2 km below the original surface, seen in deep valleys, the lavas and breccias are affected by strong chloritisation and zeolitisation, and the fractures are sealed with secondary minerals (Rançon 1985). On outcrops at this depth, mainly low-angle zones of breccia and low-angle faults are found, accompanied by sills and outwardly inclined dykes (Figs. 10, 11). Some of the intrusions have highly lobate margins, indicating slow intrusion into ductile country rock, and some of the faults have ductile features, such as schistosity development and foliation (e.g. Famin and Michon 2010). The interface between brittle and ductile structural features is diffuse, and brittle features found alongside ductile features, such as the inclined straight-sided dykes and lobate dykes (Fig. 10), indicate a strain rate dependence of the deformation. The inclined dykes also indicate a probable outwards sliding of the upper part of the edifice that could be interpreted as sector collapse (Famin and Michon 2010) or spreading-

related displacement, or a combination. The brittle–ductile interface is also marked in the Salazie Cirque by the outcrop of the top of gabbroic bodies, with highly deformed upper contracts, beautifully described by Famin and Michon (2010).

Geophysical data can be used to determine the extent of the intrusive bodies on Piton des Neiges. Figure 9c combines the shaded relief image with gravimetric data. There is a strong positive gravity anomaly at the centre of the edifice that can be clearly linked a dense intrusive complex (Fig. 9d; Gailler and Lénat 2010). Three-dimensional gravity and magnetic modelling shows a flattened laccolith shape with a central peak. The modelled 3D and plan view shapes of this intrusive complex are similar to the type 1 intrusions observed in the models (Fig. 4b). Furthermore, the gravity modelling-derived intrusive complex shape has branches that coincide with the Cirques and escarpments observed in the topography, suggesting an intimate link between the intrusion shape and the inferred structural pattern, a feature also seen in the models.

Fig. 9 a Digital Elevation Model of La Reunion Island and submarine flanks. This image shows the star-shaped central part of Piton des Neiges in the context of the broad submarine flanks that make up the greatest part of the edifice. Note that the star graben-like topography stops at sea level, roughly at about the same altitude as brittle–ductile transition level observed in the eroded edifice. The outer submarine edifice is composed of less coherent sediments, debris avalanche deposits and hyaloclastites (e.g. Oehler et al. 2005) that may accommodate the outward spreading either on strike-slip faults or by diffuse folding. The recent sediments and clastic deposits would also tend to mask such structures. **b** Image of the subaerial part of the island with the major escarpments indicated. Note the star-shaped pattern over Piton des Neiges (PdeN) and the horseshoe shape of Piton de la Fournaise (PdeF). **c** Topography of La Réunion island with the draped Bouger gravity anomaly. This shows the close association between the gravity anomaly and the star-shaped pattern of escarpments on Piton des Neiges. **d** 3D view of the modelled Piton des Neige intrusion from Gailler and Lénat (2010). Coloured scale in metres. This shows that the shape of the intrusion has a similar upper shape to the type 1 intrusions created in the models
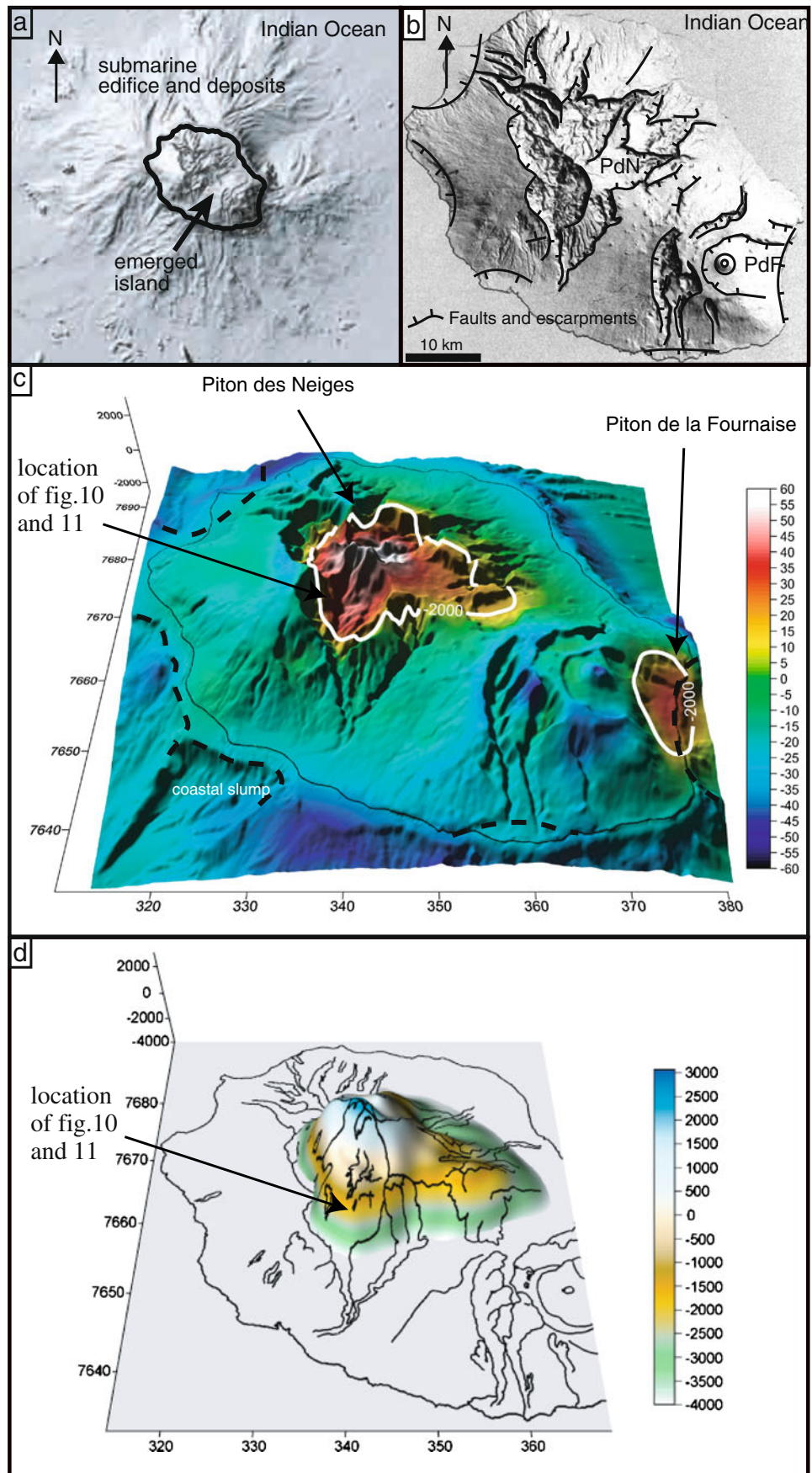
Fig. 10 Field images and sketches of the structure in Piton des Neiges. **a** Example of the intensely fractured interior of Piton des Neiges. This outcrop shows a lave sequence, intruded by dykes, which has been intensively brecciated. Note the brecciated dyke *above* scale person's head and dipping brecciated lava flow core in the *centre* of the image. **b** Brecciated thrust zone near to the outcrop in **a**, showing steeply dipping lavas, cut by low-angle thrust, that is intruded above by a low-angle intrusion. Similar geometries are also reported by Famin and Michon (2010). **c** Low-angle sheared dyke (in *pink*) intruded into lava sequence. The shear zone probably predated the intrusion, but the intrusion has also been deformed within the shear zone
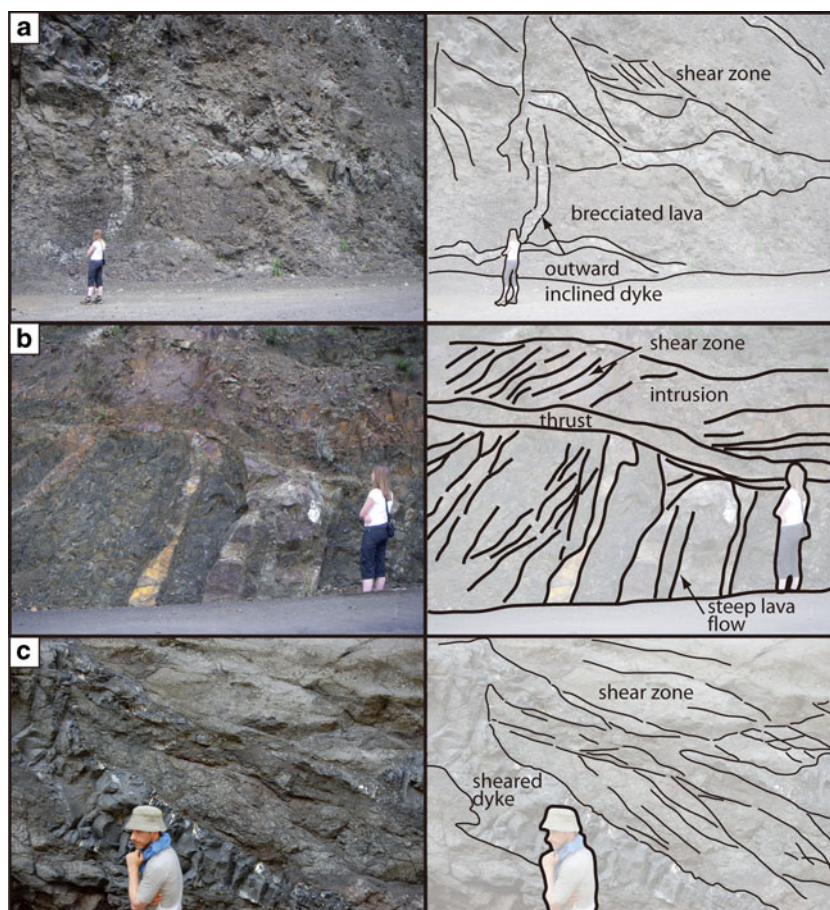
The morphology of the intrusive complexes that have been formed during our experiments thus replicates well the intrusion shape observed in Piton des Neiges. In addition, the relationships between the intrusion shape and the structures are similar. The position of the intrusion is also within the ductile altered and brecciated volcanic layers. There is extreme fracturing in the central part of both the models and in the natural example. We propose that, similar to our model, the graben structures and fracturing observed around the Piton des Neiges are linked to the spreading of the edifice and to the growth and spreading of the intrusive complex (Fig. 9c, d). The spreading of Piton des Neiges would have occurred principally during the formation of the intrusive complex, and the displacement would have been accommodated at or below sea level by the outward movement of the volcano flanks (Fig. 12). The many of the coastal and submarine debris avalanches mapped around Piton des Neiges (e.g. Oehler et al. 2005) could have been triggered by this outward displacement that would steepen the submarine flanks. These steep and avalanching structures are seen also in the models where they could be considered as the equivalent of La Réunion coastal scarps. The debris avalanches may have covered

spreading-related thrust faults, such as those seen below the Hilina slump in Hawaii (Morgan et al. 2003). Or, as the flanks of Piton des Neiges are quite shallowly dipping, thrusts may not have formed, but the graben may have rather transferred deformation to strike-slip faults that would leave little topographic expression (Delcamp et al. 2008).

Piton de la Fournaise

The structures interpreted from outcrop and topography on Piton de La Fournaise (e.g. Upton and Wadsworth 1965; Merle et al. 2010) do not have a radial pattern like on Piton des Neiges, but rather have a series of horseshoe-shaped faults, superimposed on some caldera-like depressions surrounded by flatter benches (Fig. 9b). The calderas have been interpreted as magmatic calderas (Bachèlery 1981), as hydrothermal calderas (Merle and Lénat 2003) or were related to a combination of basement fault reactivation and hydrothermally altered layers (Michon et al. 2007). While no large gravity high is associated with the main cone of Piton de la Fournaise, a major high is sited at the east coast (called the Grand Brulé anomaly; Malengreau et al. 1999; Gailler 2010) that is known from exploratory drill cores to
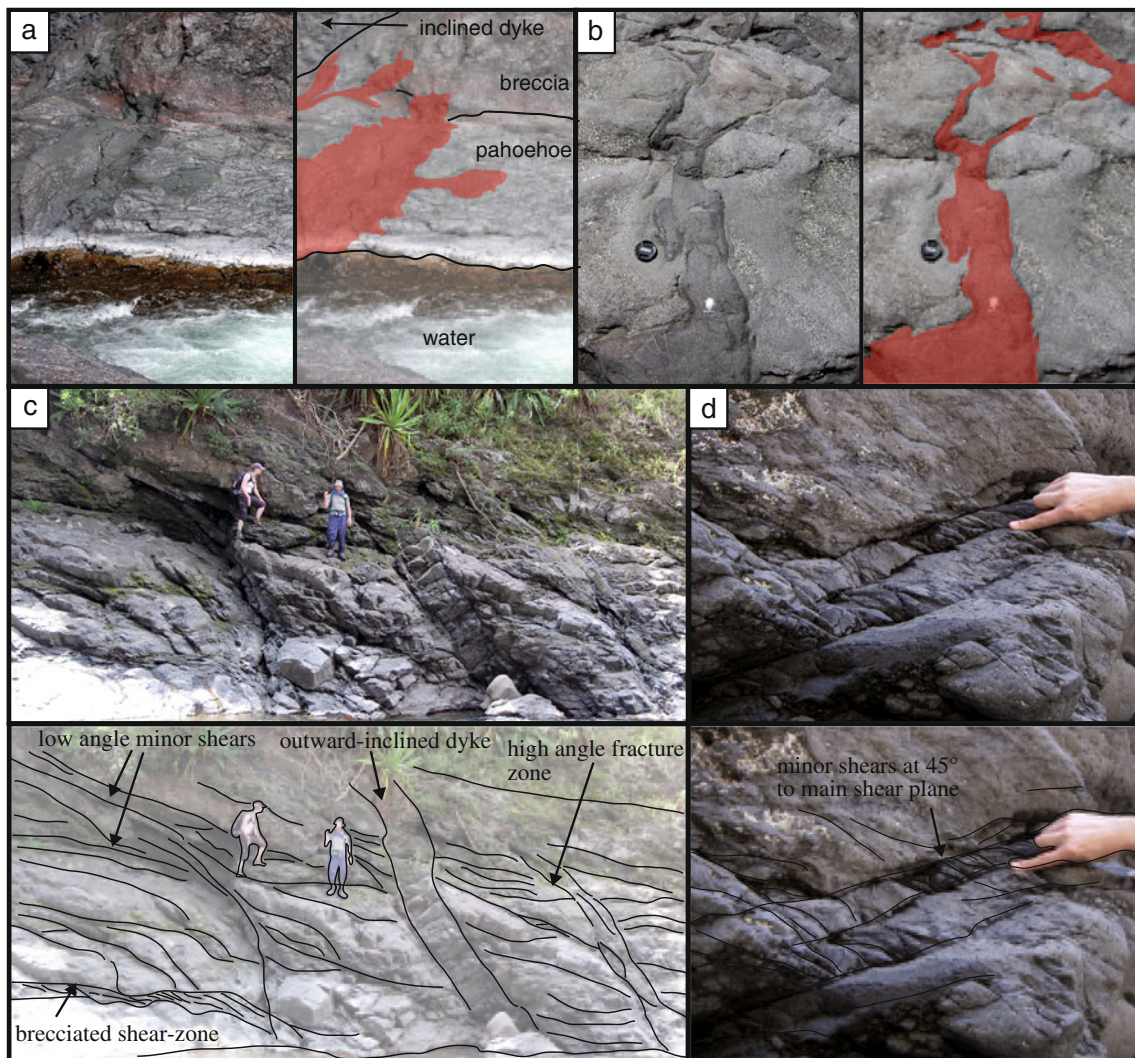
Fig. 11 a Example of a lobate sided dyke intruded into ductile pahoehoe and breccia sequence with intense chloritisation and zeolitisation. On the extreme *top left* of the image, a more recent straight-sided low-angle dyke cuts the sequence. **b** Example of lobate dykes intruded into altered pahoehoe lavas. **c** Low-angle fault zones with higher angle straight-sided dykes. **d** Detail of the shear fracture in a low-angle shear zone

be a dense gabbroic body (Rançon et al. 1987; Rançon 1990). Also, there is a north–south elongated gravity high to the west of the active cone under the Plaine des Sables (Gailler et al. 2009).

The structural pattern seen could be consistent with sector spreading, as originally suggested by Upton and Wadsworth (1965), and the geometry looks similar to the L3 model of this study (Fig. 2b). The upper Plaine des Sables gravity anomaly fits the location and geometry that an intrusive complex associated with the Plaine des Sables fault would have, according to the models. The Grand Brûlé anomaly is thought to be associated to an older edifice, the Alizés volcano, and its relationship to the present topography is not clear.

The present rift zone that extends to the north and south of Dolomieu crater may be a manifestation of an elongated intrusion that is developing at depth. While there is no clear gravity evidence for this, the deformation data show that there is a body at depth (around sea level), and recent eruptions have produced highly crystal-rich lavas that may represent the partial destruction of the intrusive complex. Also, ground deformation data (e.g. Froger et al. 2004) indicate large-scale displacement of the seaward flank towards the sea. While much of this displacement could be attributed to shallow dyke emplacement, the underlying cause could be sector spreading and intrusion development that is partly accommodated by dyke intrusion. The dykes may record the rapid intrusion events in the context of generally slow seaward spreading, and they could be the equivalent of the inclined straight dykes seen in Piton des Neiges (Fig. 11).
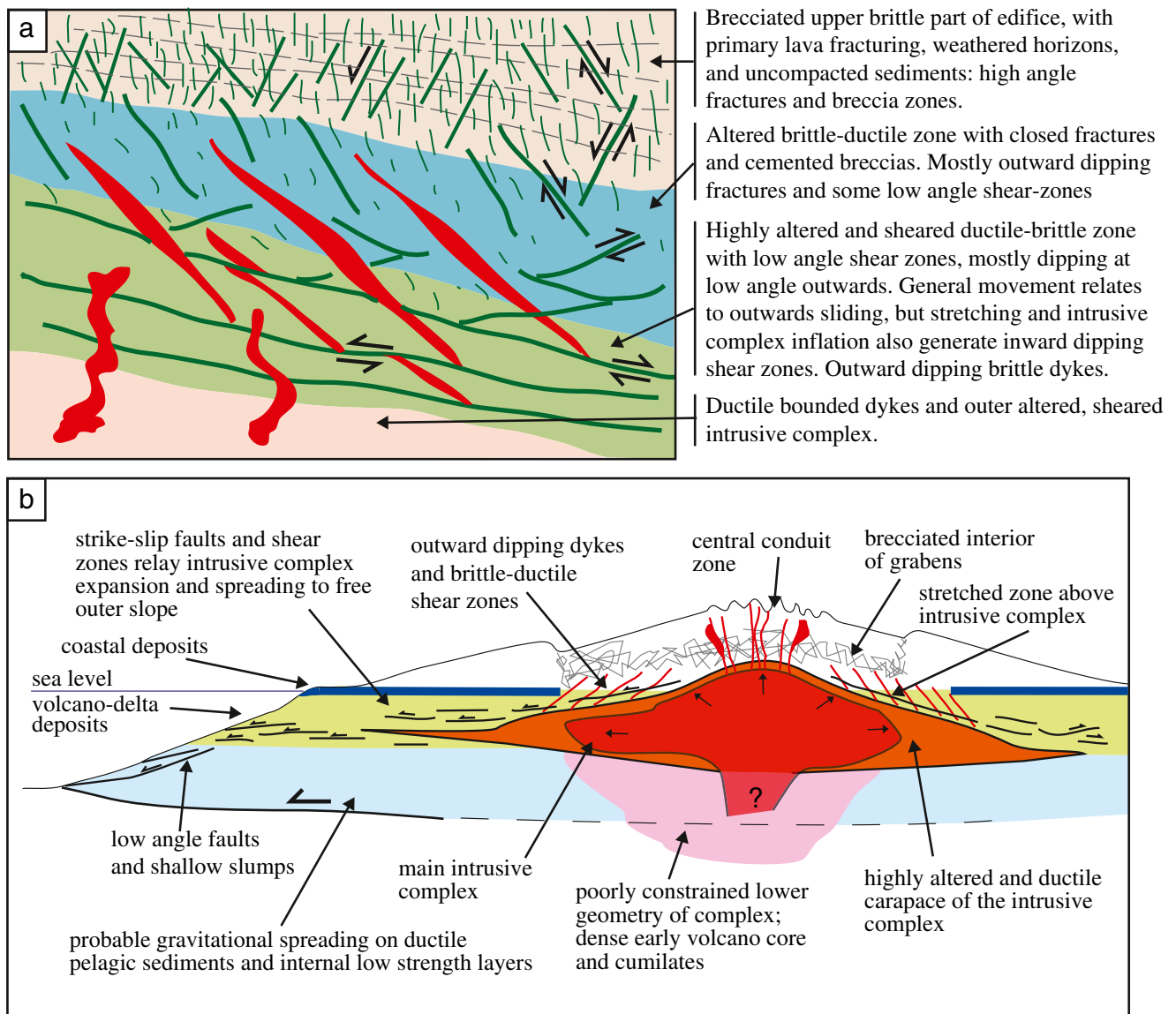
Fig. 12 a Sketches of low-angle deformation in Piton des Neiges. **b** Summary cross section of Piton des Neiges with associated deformation. This shows the large intrusive complex, shaped like a laccolith with a slightly dome top. It shows the brecciated and altered rock around the intrusion and the graben structures, as well as the low-angle slide planes that accommodate the outward intrusion push and spreading. The submarine flanks of the volcano provide an open boundary for the deformation to disperse, and flank steepening is accompanied by slumping and landsliding, although many structures are obscured by debris avalanches and sediments derived from the rapid erosion of the island. Piton de la Fournaise would have a similar structure, but is asymmetric

Conclusions

A volcano based on a ductile basal layer will slowly spread leading to the formation of grabens and en echelon faults. The analogue models performed in this study show that adding an intrusion into a spreading volcano does not significantly change the structural pattern: no distinctive and diagnostic new structures are formed. A simple structural analysis is thus not sufficient to differentiate the spreading of a ductile substratum from the spreading of an intrusive complex. Fortunately, deformation fields greatly

differ, and the role of intrusive complex emplacement within a spreading volcano can be constrained in the field with deformation or gravity measurements. In addition, the spreading of an intrusive complex in a spreading volcano can be observed if the complex is offset from the volcano summit as observed in our models and possibly at Maderas volcano.

Shallow and small intrusive complexes were modelled here (0.1 to 0.2 km^3). Their morphology depends essentially on the thickness of the brittle layering. Without this layer, intrusive bodies were circular with a bulged summit

and a cylindrical base. For a brittle layer thickness equal or greater than the ductile layer, the complex propagated and spread as elongated branches that followed a transversal graben. A complex that is emplaced into a spreading volcano will thus more likely propagate horizontally than vertically. The horizontal propagation can favour rift zone development, and can drive flanks sideways, to create slumps and possible sector collapse.

In the analogue models, horizontal displacements due to substratum spreading were increased when the intrusive fluxes were higher. This observation indicates that spreading of ductile substrata and intrusive complex are intimately linked. These two processes can play together or operate at different times, one triggering and/or favouring the other.

The experiments show that the three-armed rift zone, a typical feature of oceanic islands, is associated with sector spreading that are due to (1) a presence of a thick brittle edifice layer and (2) the irregularly and variability of this layer. A thicker brittle layer (1) reduces the number of grabens to obtain the three-armed feature, whereas the asymmetry (2) promotes the sector spreading.

A good relationship has been achieved between natural cases and our models, using field and geophysical evidence. We have interpreted the geology and structure of La Réunion island in terms of the development of a major intrusive complex for Piton des Neiges, with associated intense brecciation and the formation of a star-shaped set of graben. The lateral spreading of this volcano may have been responsible for the large number of debris avalanches seen on the submarine flanks. For Piton de la Fournaise, there has probably been sector spreading, and the interpreted intrusive bodies in the volcano fit this hypothesis. Their present rift zone may be evidence of a developing intrusive complex below the summit, but elongated north–south, like the earlier Plaine des Sables body. This study lays the ground to reinterpret volcanic and intrusive structures in terms of coupled gravity and magma intrusion tectonics and provides information that can be used to distinguish such processes on active volcanoes.

References

Annen C, Lénat JF, Provost A (2001) The long-term growth of volcanic edifices: numerical modeling of the role of dyke intrusion and lava-flow emplacement. J Volcanol Geotherm Res 105:263–289

Arnaud N (2005) Les Processus de démantèlement des volcans, cas d'un volcan bouclier en milieu océanique : Le Piton des Neiges (île de La Réunion). PhD Thesis, Université de La Réunion, Saint Denis

Bachèlery P (1981) Le Piton de la Fournaise (Ile de la Réunion): étude volcanologique, structurale et pétrologique. PhD Thesis, Université Blaise Pascal, Clermont-Ferrand

Bailey EB, Clough CT, Wright WB, Richey JE, Wilson GV (1924) Tertiary and post-tertiary geology of Mull Loch Aline and Oban. British Geological Survey. Mem Geol Surv Great Brit 44:172–184

Beauducel F, Cornet FH, Suhanto E, Duquesnoy T, Kasser M (2000) Constraints on magma flux from displacements data at Merapi volcano, Java. J Geophys Res 105:8193–8204

Borgia A (1994) Dynamic basis of volcano spreading. J Geophys Res 99:17791–17804

Borgia A, van Wyk de Vries B (2003) The volcano-tectonic evolution of Concepción, Nicaragua. Bull Volcanol 65:248–266

Borgia A, Burr J, Montero W, Morales LD, Alvarado GE (1990) Fault-propagation folds induced by gravitational failure and slumping of the Central Costa Rica volcanic range: implications for large terrestrial and Martian volcanic edifices. J Geophys Res 95:14,357–14,382

Borgia A, Ferrari L, Pasquarè G (1992) Importance of gravitational spreading in the tectonic and volcanic evolution of Mount Etna. Nature 357:231–235

Borgia A, Delaney PT, Denlinger RP (2000) Spreading volcanoes. Annu Rev Earth Planet Sci 28:3409–3412

Brooks BA, Foster J, Sandwell D, Wolfe CJ, Okubo P, Poland M, Myer D (2008) Magmatically triggered slow slip at Kilauea Volcano, Hawaii. Science 321(5893):1177

Carena S, Borgia A, Pasquarè G, Battaglia A, Ferraris M, Martelli L, De Nardo MT (2000) Gravity synclines. J Geophys Res 105:21,819–21,833

Cayol V, Dieterich JH, Okamura AT, Miklius A (2000) High magma storage rates before the 1983 eruption of Kilauea, Hawaii. Science 288:2343. doi:10.1126/science.288.5475.2343

Cecchi E (2003) Reconstruction 3D pour la volcanologie : apports d'une méthode multi-vues par photogrammétrie numérique. PhD Thesis, Université B.Pascal, Clermont-Ferrand, pp. 132–134

Chiocci FL, Coltelli M, Bosman A, Cavallaro D (2011) Continental margin large-scale instability controlling the flank sliding of Etna volcano. Earth Planet Sci Lett 305:57–64

Clague DA, Denlinger RP (1994) Role of olivine cumulates in destabilizing the flanks of Hawaiian volcanoes. Bull Volcanol 56:425–434

Delaney PT, Fiske RS, Miklius A, Okamura AT, Sako M (1990) Deep magma body beneath the summit and rift zones of Kilauea Volcano, Hawaii. Science 247:1311–1346

Delcamp A, van Wyk de Vries B, James MR (2008) The influence of edifice slope and substrata on volcano spreading. J Volcanol Geotherm Res 177:925–943

Dieterich JH (1988) Growth and persistence of Hawaiian volcanic rift zones. J Geophys Res 93:4258–4270

Donnadieu F (2000) Déstabilisation des édifices volcaniques par les cryptodômes: modélisation analogîque et approche numérique. PhD Thesis, Université B.Pascal, Clermont-Ferrand, p. 39

Famin V, Michon L (2010) Volcano destabilization by magma injections in a detachment. Geology 38:219–222

Francis P, Oppenheimer C, Stevenson D (1993) Endogenous growth of persistently active volcanoes. Nature 366:554–557

Froger JL, Fukushima Y, Briole P, Staudacher T, Souriot T, Villeneuve N (2004) The deformation field of the August 2003 eruption at Piton de la Fournaise, Reunion Island, mapped by ASAR interferometry. Geophys Res Letters 31:L14601, 5 PP

Fukushima Y, Cayol V, Durand P (2005) Finding realistic dike models from interferometric synthetic aperture radar data: the February

2000 eruption of Piton de la Fournaise. J Geophys Res 110. doi:10.1029/2004JB003268

Gailler LS (2010) Structure interne d'un système volcanique océanique de type point chaud, La Réunion: Approches géophysiques. PhD thesis, University B. Pascal, Clermont-Ferrand

Gailler LS, Lénat JF (2010) Three-dimensional structure of the submarine flanks of La Réunion inferred from geophysical data. J Geophys Res B: Solid Earth 115:B12105

Gailler LS, Lénat JF, Lambert M, Levieux G, Villeneuve N, Froger JL (2009) Gravity structure of Piton de la Fournaise volcano and inferred mass transfer during the 2007 crisis. J Volcanol Geotherm Res 184:31–48

Hasenaka T, Carmichael ISE (1985) The cinder cone of Michoacan-Guanajauto, Central Mexico: their age, volume, distribution and magma discharge rate. J Volcanol Geotherm Res 25:105–124

Hill DP, Zucca JJ (1987) Geophysical constraints on the structure of Kilauea and Mauna Loa volcanoes and some implications for seismomagmatic processes. U.S. Geol Surv Prof Pap 1350 pp 903–917

Holohan EP, van Wyk de Vries B, Troll VR (2008) Analogue models of caldera collapse in strike-slip tectonic regimes. Bull Volcanol. doi:10.1007/s00445-007-0166-x

Hubbert MK (1937) Theory of scale models as applied to the study of geologic structures. Bull Geol Soc Am 48:1459–1520

Kauahikaua J, Hildenbrand TG, Webring M (2000) Deep magmatic structures of Hawaiian volcanoes; imaged by three-dimensional gravity models. Geology 28(10):883–886

Lebas E (2009) Genèse et nature de la fracturation des édifices volcaniques: de l'échelle du volcan à l'échelle de la coulée. Ms Thesis, University B. Pascal, Clermont-Ferrand, p. 51

Lénat JF, Gibert-Malengreau B, Galdeano A (2001) A new model for the evolution of the volcanic island of Réunion (Indian Ocean). J Geophys Res B106(5):8645–8663

Malengreau B, Lénat JF, Froger JL (1999) Structure of Réunion Island (Indian Ocean) inferred from the interpretation of gravity anomalies. J Volcanol Geotherm Res 88:131–146

Marsh BD (1981) On the crystallinity, probability of occurrence, and rheology of lava and magma. Contrib Mineral Petrol 78:85–98

Mathieu L, van Wyk de Vries B (2009) Edifice and substrata deformation induced by intrusive complexes and gravitational loading in the Mull volcano (Scotland). Bull Volcanol 71 (10):1133–1148

Mathieu L, van Wyk de Vries B, Holohan EP, Troll VR (2008) Dykes, cups, saucers and sills: analogue experiments on magma intrusion into brittle rocks. Earth Planet Sci Lett 271(1–4):1–13

McNight SB, Williams SN (1997) Old cinder cone or young composite volcano? The nature of Cerro Negro, Nicaragua. Geology 25:339–342

Merle O, Borgia A (1996) Scaled experiments of volcanic spreading. J Geophys Res 101:13,805–13,817

Merle O, Lénat JF (2003) Hybrid collapse mechanism at Piton de La Fournaise volcano, Réunion Island, Indian Ocean. J Geophys Res 108(B3):2166

Merle O, Vendeville B (1992) Modélisation analogique de chevauchements induits par des intrusions magmatiques. C R Acad Sci Paris 315(série II):1541–1547

Merle O, Mairine P, Michon L, Bachèlery P, Smietana M (2010) Calderas, landslides and paleo-canyons on Piton de la Fournaise volcano (La Réunion Island, Indian Ocean). J Volcanol Geotherm Res 189:131–142

Michon L, Saint-Ange F (2008) Morphology of Piton de la Fournaise basaltic shield volcano (La Réunion Island): characterization and

implication in the volcano evolution. J Volcanol Geotherm Res 113(B03203):1–19

Michon L, Saint-Ange F, Bachèlery P, Villeneuve N, Staudacher T (2007) Role of the structural inheritance of the oceanic lithosphere in the magmato-tectonic evolution of Piton de la Fournaise volcano (La Réunion Island). J Geophys Res 112: B04205

Middleton GV, Wilcock PR (1994) Mechanics in the Earth and environmental sciences. Cambridge University Press, Cambridge

Mogi (1958) Relation between the eruptions of various volcanoes and deformations of the ground surfaces around them. Bull Earth Res Inst 36:99–134

Morgan JK, McGovern PJ (2005) Discrete element simulations of gravitational volcanic deformation: 1. Deformation structures and geometries. J Geophy Res 110:B05402. doi:10.1029/2004JB003252

Morgan JK, Moore GF, Clague DA (2003) Slope failure and volcanic spreading along the submarine south flank of Kilauea volcano, Hawaii. J Geophy Res 108:24–15. doi:10.1029/2003JB002411

Münn S, Walter TR, Klügel A (2006) Gravitationnal spreading controls rift zones and flank instabilities on El Hierro, Canary Island. Geol Mag 143(3):257–268

Murase T, McBirney AR (1973) Properties of some common igneous rocks and their melts at high temperatures. Bull Geol Soc Amer 84:3563–3592

O'Driscoll B, Troll VR, Reavy J, Turner P (2006) The Great Eucrite intrusion of Ardnamurchan, Scotland: re-evaluation of the ring-dyke concept. Geology 34:189–192

Oehler JF, van Wyk de Vries B, Labazuy P (2005) Landslides and spreading of oceanic hot-spot and arc shield volcanoes on Low Strength Layers (LSLs): an analogue modeling approach. J Volcanol Geotherm Res 144(1–4):169–189

Okada Y (1992) Internal deformation due to shear and tensile faults in a half-space. Bull Seism Soc Am 82:1018–1040

Okubo S, Watanabe H (1989) Gravity change caused by a fissure eruption. Geophys Res Lett 16:445–448

Okubo PG, Benz HM, Chouet BA (1997) Imaging the crustal magma sources beneath Mauna Loa and Kilauea volcanoes, Hawaii. Geology 25:865–870

Ramberg H (1981) Gravity, deformation and the Earth's crust in theory, experiments and geologic application, vol 2. Academic, London, p 452

Rançon JP (1985) Hydrothermal history of Piton des Neiges volcano (Réunion Island, Indian Ocean). J Volcanol Geotherm Res 26:297–315

Rançon JP (1990) Lithostratigraphie du forage du Grand Brûlé. Implications volcanologiques. In: Lénat JF (ed) Le volcanisme de la Réunion. Monographie. Centre de Recherches Scientifiques, Clermont-Ferrand, pp 187–200

Rançon JP, Lerebour P, Auge T (1987) Mise en évidence par forage d'une chambre magmatique ancienne à l'aplomb de la zone orientale du Piton de La Fournaise (Ile de La Réunion). Implications volcanologiques. CR Acad Sc Paris 304:55–60

Robson S, Shortis MR (2004) Visual Measurement System. http://www.geomsoft.com

Roche O, van Wyk de Vries B, Druitt TH (2001) Sub-surface structures and collapse mechanisms of summit pit craters. J Volcanol Geotherm Res 105:1–18

Rosenberg CL (2001) Deformation of partially molten granite: a review and comparison of experimental and natural case studies. Int J Earth Sciences 90:60–76

Swanson DA, Duffield WA, Fiske RS (1976) Displacement of the south flank of Kilauea Volcano: the result of forceful

intrusion of magma into the rift zone. US Geol Surv Prof Pap 963:39

Tyrell GM (1928) The geology of Arran. PhD Thesis, Glasgow University, British Geological Survey

Upton BGJ, Wadsworth WJ (1965) Geology of Réunion Island, Indian Ocean. Nature 207:151–154

Van Bemmelen RW (1949) The geology of Indonesia: general geology of Indonesia and adjacent archipelagos. Government Printing Office, The Hague

van Wyk de Vries B, Matela R (1998) Volcano-induced deformation: numerical models of substratum flexure, spreading and extrusion. J Volcanol Geotherm Res 81:1–18

van Wyk de Vries B, Cecchi E, Robineau B, Merle O, Batchèlery P (2001) Factors governing the volcano-tectonic evolution of La

Réunion Island: a morphological, structural and laboratory modelling approach. Journal of Conference Abstracts 6:800

Wadge G (1982) Steady state of volcanism: evidence from eruptive histories of polygenetic volcanoes. J Volcanol Geotherm Res 87:4035–4039

Walter TR, Klügel A, Münn S (2006) Rift zone formation on overlapping volcanoes by gravitational spreading. Terra Nova 18:26–33

Wicks CW, Dzurisin D, Ingebritsen S, Thatcher W, Lu Z, Iverson J (2002) Magmatic activity beneath the quiescent Three Sisters volcanic center, central Oregon Cascade range, USA. Geophys Res Let 29:10–1029

Wooller L, van Wyk de Vries B, Murray JB, Rymer H, Meyer S (2004) Volcano spreading controlled by dipping substrata. Geology 32(7):573–576